
BENEMÉRITA UNIVERSIDAD AUTÓNOMA DE PUEBLA
FACULTAD DE CIENCIAS FÍSICO MATEMÁTICAS

# Partial wave analysis for central pions produced in diffractive events with ALICE at LHC

Thesis presented as a partial requirement for obtaining the degree of **Master in Science Applied Physics**

Presented by

**Irandheny Yoval Pozos**

Supervised by

**Ph. D. Mario Rodríguez Cahuantzi**

Puebla , Mexico July 2022

**Title:** Partial wave analysis for central pions produced in diffractive events with ALICE at LHC.

**Student:** Irandheny Yoval Pozos

COMMITTEE

---

Ph. D. Cristian Heber Zepeda Fernández

President

---

Ph. D. Héctor Novales Sánchez

Secretary

---

Ph. D. Arturo Fernández Téllez

Member

---

Ph. D. Enrique Varela Carlos

Alternate

---

Ph. D. Mario Rodríguez Cahuantzi

Advisor

## Abstract

ALICE is an experiment designed primarily for the study of matter under extreme conditions of temperature and energy density, located at one of the interaction points of the LHC at CERN. Due to its design characteristics, with ALICE it is possible to collect diffractive events in proton-proton collisions. In this work we present the analysis of central production events with 2 and 4 pions. The technique known as partial wave analysis is used to give an interpretation of the angular distributions of 2 and 4 pion events within the Collins-Soper reference frame for the diffractive events collected by ALICE during the Run 2 of LHC for proton+proton collisions at 13 TeV assuming a contribution of the $f_2(1270)$ resonance..

## Acknowledgements

I want to thank my mother for giving me unconditional love and support throughout my life. To Dr. Mario Rodríguez Cahuantzi for guiding and supporting me during the completion of this thesis work. To CONACyT for the master's scholarship and the support with the CONACyT project A1-S-13525, as well as, the Laboratorio Nacional de Supercómputo del Sureste.

To my mother

# Contents

# List of Tables

# List of Figures

# Chapter 1

# Introduction

ALICE is one of the four main experiments located at CERN's LHC, located on the French-Swiss border, which focuses on the study of the nuclear matter created in proton-proton and heavy-ion collisions, i.e. extreme conditions of temperature and energy density [6]. The trigger of ALICE was configured to identify and collect, diffractive processes in proton-proton collisions are experimentally characterized by pseudorapidity gaps.

With data collected between 2009 and 2014, ALICE reported the measurement of the cross sections for elastic, inelastic and diffractive in proton-proton collisions at centre of mass energy $\sqrt{s} = 0.9, 2.7 and 7$ TeV [5]. The fractions of diffractive processes in inelastic collisions were calculated from a detailed study of the space gaps (rapidity gaps) in terms of the pseudorapidity distributions of particles produced in proton-proton collisions. The cross sections for single and double diffraction reported by ALICE are:

$$\sigma_{SD} = 12.2^{+3.9}_{-5.3}(syst) mby \sigma_{DD} = 7.8 \pm 3.2(syst) mba \sqrt{s} = 2.76 TeV$$

$$\sigma_{SD} = 14.9^{+3.4}_{-5.9}(syst) mby \sigma_{DD} = 9.0 \pm 2.6(syst) mba \sqrt{s} = 7 TeV$$

The determination of these cross sections was carried out by quantitative estimation of the combination of the relative frequencies of the number of diffractive process

events identified by the ALICE trigger system with the inelastic cross sections. This result showed the capabilities of the ALICE trigger system for the identification and characterization of diffractive processes in proton-proton collisions at LHC energies.

Diffractive processes were introduced to high energy physics in the 1950's by a group of physicists including Robert Serber, Roy J. Glauber, Evgeniy L. Feinberg, Isaak Pomeranchunk, among others. Hadronic cross sections at high energies are usually described by Regge theory [9]. These phenomena in proton-proton collisions represent more than 25% of the effective cross section of the collision [19]. These collisions are dominated by a low transferred momentum, so the study of them shows an opportunity to deepen the knowledge of the proton structure, as well as of the non-perturbative processes of QCD.

The study of the central production (CEP) diffractive processes can be performed with the partial wave analysis technique [13]. To make use of this tool it is necessary to consider a reference system where the angular dependence of the differential cross section is proportional to $(1+\cos^2(\theta))$. This is the case of the Collins-Soper framework [16], from which it is possible to study the decay processes ranging from two to N bodies, as well as the resonances $f_0(980)$, $f_0(1710)$ and $f_0(1270)$.

Partial wave analysis (PWA) is a tool used to describe scatering process at quantum level. We know the expansion of the total amplitude, which can be decomposed into a sum of partial waves [10, 12, 20]. The PWA has a direct connection with the optical theorem, which establishes the relationship between the cross-section and the scattering amplitude. For this reason it is also possible to estimate the contribution of each partial wave in terms of the cross section [13].

In this thesis an angular study of central production events in diffractive processes for 2 and 4 pions in the Collins-Soper reference frame is presented. A discussion of the partial wave formalism is also discussed using the previous ALICE results for 7 TeV.

# Chapter 2

# Theoretical framework

## 2.1 Diffractive Processes

The study of diffractive processes was introduced by Robert Serber, Roy J. Glauber, Isaak Pomeranchunk, Evgeniy L. Feinberg, to mention a few [19]. The precedent studies in diffraction phenomena were carried out by Leonardo Da Vinci in 16th century and Francesco Maria Grimaldi in 1665. The study of diffractive processes in high energy physics is analogous to the phenomenon that occurs with the diffraction of light.

The diffractive processes in proton-proton collisions represent more than twenty-five percent of the collision cross section [19], in addition to the fact that these collisions are dominated by a low transferred momentum, so the study of them represents an opportunity to deepen the knowledge of the proton structure, as well as of the non-perturbative processes of QCD [19]. On the other hand, it is important to stress that hadronic cross sections at high energies are usually described under the Regge theory [9], through the exchange of pomerons.

The first definition of hadronic diffraction was established by Good and Walker, in 1960, where they point out that "A phenomenon is predicted in which a high energy particle beam undergoing diffraction scattering from a nucleus will acquire components corresponding to various products of the virtual dissociations of the incident parti-

cle[...] These diffraction-produced systems would have an extremely narrow transverse momentum distribution and would have the same quantum numbers of the initial particle" [8].

Hadronic diffraction is usually defined as a process where there's not interchange of quantum numbers in the collision. In addition, there must be a conservation of quantum numbers between the incident and resulting particles, so this process occurs at high energies [8], these diffractive reactions from the definition proposed by Good and Walker can be classified as follows:

- Elastic Scattering, the incident and produced particles are the same.

$$P_1 + P_2 \longrightarrow P_1^{'} + P_2^{'}$$

- Single Diffraction, in the final state of the collision one of the incident particles leaves intact, while the other dissociates producing new particles, conserving the same quantum numbers.

$$P_1 + P_2 \longrightarrow P_1^{'} + X$$

- Double Diffraction, in the final state of the collision, the incident particles dissociate, thus generating new particles that conserve the same quantum numbers as the incident particles.

$$P_1 + P_2 \longrightarrow X_1 + X_2$$

- Central Diffraction, the resulting particles in the final state of the collision correspond to the incident ones, but there is also a production of particles given by the double pomeron exchange.

$$P_1 + P_2 \longrightarrow P_1^{'} + X + P_2^{'}$$

where X represents the other particles produced by the dissociation of the initial particles, as well as, those originating from the double pomeron exchange.

Diffractive processes have the characteristic of always conserving the quantum numbers before and after the collision. The following image shows the four Feynman diagrams of the diffractive processes that we can study in proton-proton collisions, it is important to note that the present work focuses on the study and analysis of the central diffractive processes.

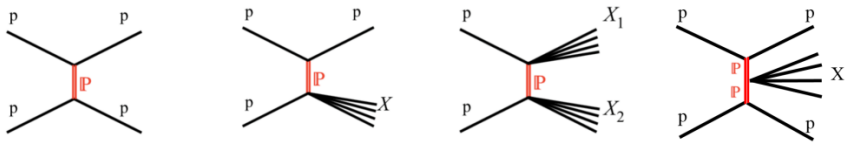


Figure 2.1: Feynman diagrams for diffractive processes representing pomeron exchanges. From left to right, elastic scattering, single diffraction, double diffraction and central diffraction. [24]

From the experimental point of view, the definition given by Good and Walker presents a limitation, since the final state of the collision may not be reconstructed in its entirety, we would not know if there is conservation of quantum numbers with respect to the initial state, therefore, it is essential for the study of these phenomena to establish an experimental definition that meets the requirements of these processes established in 1960.

The equivalent definition used for the experimental study of these processes states that: "A diffractive reaction is characterized by a large, non-exponentially suppressed, rapidity gap in the final state" [8], which indicates that a diffractive process is characterized by the presence of rapidity gaps between the particles produced after the collision, in the case of the central diffraction there is a double gap in the final state, as shown in Figure 2.1 .

The theory that focuses on the study of diffractive phenomena is known as Regge Theory, which explains in general terms how these phenomena are dominated by the exchange of pomerons between the incident particles when interacting with each other. To speak of diffraction within this theoretical framework is a direct reference to the physics of pomerons, as well as to the exchange of vacuum quantum numbers.

## 2.2 Kinematic Variables

The study of diffractive processes from the experimental point of view focuses on the analysis of the final states of the collision, since these states present specific or very particular kinematic considerations. In this chapter, generalities of the kinematic variables of diffractive phenomena are presented.

### 2.2.1 Mandelstam's variables

Mandelstam variables are commonly used for the description of processes in which we have two incoming particles in the initial state and two particles in the final state, the conservation of momentum is expressed as $p_1 + p_2 = p_3 + p_4$, where $p_1$ and $p_2$ refer to the moments of particles 1 and 2 respectively before the collision, while $p_3$ and $p_4$ are the moments of particles 3 and 4 respectively after the collision. From these 4-moments it is possible to establish a relation between the momentum and the invariant mass of the i-particle, given by $p_i^2 = m_i^2$ for $i = 1, 2, 3, 4$, from which we have 8 constraints.

"Altogether, this gives us $4x4 - 8 = 8$ independent momentum variables, and the number of independent Lorentz-invariant combinations of these variables is only $8-6 = 2$ " [25], which correspond to the two degrees of freedom of the system that are related to the energy of the center of mass and the scattering angle of the particles. It is convenient to use three independent Lorentz variables, which are called Mandelstam variables defined as follows:

$$s = (p_1 + p_2)^2 = (p_3 + p_4)^2$$

$$t = (p_1 - p_3)^2 = (p_2 - p_4)^2$$

$$u = (p_1 - p_4)^2 = (p_2 - p_3)^2$$

The Feynman diagrams corresponding to each of these variables are presented below Where the variable $s$ is related to "the square of the total center-of-mass (CM) energy and $t$ is the squared momentum transfer" [8], these variables satisfy the following

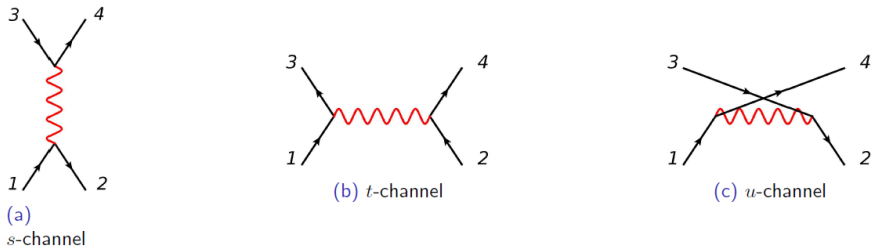


Figure 2.2: The figure on the left corresponds to the s-channel, the one in the center to the t-channel and the one on the right to the u-channel [25].

$$s + t + u = (p_1 + p_2)^2 + (p_1 - p_3)^2 + (p_1 - p_4)^2$$

$$= 3p_1^2 + p_2^2 + p_3^2 + p_4^2 + 2(p_1 p_2) - 2(p_1 p_3) - 2(p_1 p_4)$$

$$= p_1^2 + p_2^2 + p_3^2 + p_4^2 + 2p_1 \times (p_1 + p_2 - p_3 - p_4 = 0)$$

$$= p_1^2 + p_2^2 + p_3^2 + p_4^2$$

$$= m_1^2 + m_2^2 + m_3^2 + m_4^2$$

Now, consider the center-of-mass reference frame, where $p_1 + p_2 = p_3 + p_4 = 0$ and the variable $s$ relates to the collision energy of the particles, where $\sqrt{s} = E_1 + E_2 = E_3 + E_4$, while the variable $t$ parametrizes the scattering angle of the particles, through the following expression $t = -(p_3 - p_1)^2 = -p^2 \times (1 - \cos\theta)$, as a consequence, "the Lorentz-invariant definitions translate the CM-frame energy and the CM-frame scattering angle to any other frame of reference" [25].

### 2.2.2 Rapidity and Pseudorapidity

In high energy physics experiments the collisions between hadrons consider a particle of energy E that moves along the beam axis or z-axis, these processes, in a general way expose how the longitudinal momentum can acquire any value, while the transverse momentum usually takes only small values. The kinematic variable called rapidity ($y$) is employed to expose the longitudinal momentum ($p_z$).

$$y = \frac{1}{2} ln \frac{E + p_z c}{E - p_z c} \tag{2.1}$$

Equation 2.1 indicates that in the final state of a collision, if a relativistic particle results with a direction perpendicular to the beam axis then the momentum component $p_z$ will be very small so the rapidity will tend to zero, likewise, when the resulting particle has a direction along the beam axis, the rapidity will acquire a value that tends to $\pm\infty$, this relationship is clearly related to the angle of emission of the particles after the collision.

The rapidity is a kinematic variable that is transformed by the Lorentz boost along the z-axis. To demonstrate this change we start from equation 2.1 and consider an increase in $\beta$, so that $E \longrightarrow \gamma (E + \beta p_z)$ and $p_z \longrightarrow \gamma (p_z + \beta E)$ where $\gamma = \frac{1}{\sqrt{1-\beta^2}}$, thus

$$y \longrightarrow y + \frac{1}{2} log \left( \frac{1+\beta}{1-\beta} \right) = y + y_{boost} \tag{2.2}$$

So that, "any rapidity difference is invariant under longitudinal boosts and remains the same in all collinear frames" [8], likewise, in the non-relativistic limit when $v \ll 1$ occurs, we have that energy $E \longrightarrow m$ and $p_z \longrightarrow m v_z$, so the rapidity decreases, although for a particle without mass the energy $E = \mid p \mid$. This kinematic variable can be expressed in terms of the angle $\theta$, which is related to the dispersion of the particle taking as reference to the z-axis, the rapidity can be expressed as:

$$y = \frac{1}{2} ln \frac{1 + \cos\theta}{1 - \cos\theta} = -ln \tan \frac{\theta}{2} \tag{2.3}$$

From 2.3 the pseudorapidity as

$$\eta = -ln \tan \frac{\theta}{2}$$

If $\theta$ tends to zero the pseudorapidity of the particle approaches to infinity, this kinematic variable is one of the most used in studies of collisions between hadrons, because its angular dependence can be understood in terms of the phase space covered by the particle detectors in collider experiments.

It is important to note that rapidity and pseudorapidity coincide in the limit for massless particles, so that, $y \simeq \eta$ , although this can also happen when you have particles where $p_T \gg m$ or $p_z \gg m$ .

### 2.2.3 Cross section

The cross section in high-energy physics refers to the probability that some phenomenon or process will occur after a collision, and is represented by the letter $\sigma$ and is measured by effective areas (barns or millibarns), which are "are used to describe total yields of reactions regardless of energies of emitted particles or of partial distributions" [21]. It should be noted that we can find differential and double differential cross-sections, which will be discussed below.

The differential cross section, i.e., $\frac{d\sigma}{dE}$ or $\frac{d\sigma}{d\theta}$ are used to study the particle production in collider experiments by means of spatial and energy distributions. It is important to highlight those spatial or angular distributions, whose relation are given in terms of the solid angle ($\Omega$) as follows $\frac{d\sigma}{d\Omega}$ .

On the other hand, the double differential cross sections are expressed in terms of $\frac{d^2\sigma}{dEd\theta}$ and $\frac{d^2\sigma}{dEd\Omega}$ , whose units of measurement are $\frac{mb}{MeV-rad}$ and $\frac{mb}{MeV-str}$ respectively. These cross sections are studied in terms of the energy spectra and angular distribution. Experimentally, these cross sections are measured from the number of particles that were produced after the collision within the angular interval of $\theta$ y $\theta + d\theta$ , and energy range from $E$ to $E + dE$ .

Finally, it should be noted that the total cross section is invariant to the different reference frames, while the differential cross sections may or may not be invariant quantities, therefore, it is preferable to establish the differential cross sections in each of the considered reference frames.

## 2.3 Partial Wave Analysis

Partial Wave Analysis is a tool used to study scattering phenomena. This technique allows the description of the total amplitude of elastic scattering, where the total amplitude can be visualized as a decomposition of partial waves, from which one or several components of the scattering process can be described, although it is possible to decompose these waves into more partial waves, until obtaining a system that describes even the smallest partial waves [23].

The development of this technique can be carried out in various reference frames such as Collins-Soper and Gottfried-Jackson, from which it is possible to analyze decay processes ranging from two to N bodies. It is important to point out that these frameworks also allow the representation of phenomena in which the double pomeron exchange occurs.

### 2.3.1 Partial Wave Analysis Formalism

The Partial Wave Analysis formalism arises by considering particles incident on a spherically symmetric potential V(r), in which they conserve their angular momentum. In particular, in the development of the Partial Wave Analysis technique we consider that each of the waves associated to the particles is composed by a group of harmonic waves which are multiplied by a radial function.

Now, we associate a wave function to the incident particle traveling along the z-axis, which is given by

$$\psi_{inc} = e^{ikz} = e^{ikr\cos\theta}$$

This function can be expanded in terms of the coefficient $l$ to establish an angular component using spherical harmonics $Y_l^m(\theta, \phi)$ and a radial function $R(r)$, as follows

$$\psi_{inc} = \sum_{l=0}^{\infty} R(r) Y_l^m(\theta, \phi) \tag{2.4}$$

It is important to note that the spherical harmonics are solutions of the angular part of the Laplace's equation, in this case, it is necessary to choose a polar symmetry, therefore, it is essential to make the spherical harmonics independent of $\phi$ in order to express them in terms of the Legendre polynomials., i.e., $Y_l^m(\theta,\phi) = P_l(\cos\theta)$ , where $P_l(\cos\theta)$ are the Legendre polynomials, on the other hand, the radial function can be written as $R(r) = A_l J_l(kr)$ where $J_l(kr)$ represents the spherical Bessel functions and $A_l$ is a normalization factor.

We proceed to substitute $Y_l^m$ and $R(r)$ in the expression (2.4)

$$\psi_{inc} = \sum_{l=0}^{\infty} A_l J_l(kr) P_l(\cos\theta)$$

Note that the spherical Bessel functions are being considered for very large values of $r$, so that $J_l$ is given by

$$J_l(kr) = \frac{1}{kr}\sin\left(kr - \frac{l}{2}\pi\right)$$

Thus our incident wave function is as follows

$$\psi_{inc} = \frac{1}{kr}\sum_{l=0}^{\infty} A_l \sin\left(kr - \frac{l}{2}\pi\right) P_l(\cos\theta)$$

Now, we calculate the value of the normalization factor, for this we change $l$ to $n$

$$\psi_{inc} = e^{ikr\cos\theta} = \sum_{n=0}^{\infty} A_n J_n(kr) P_n(\cos\theta)$$

We multiply both sides of the equality by $P_l(\cos\theta)$ and integrate from 0 to $\pi$

$$\int_0^{\pi} e^{ikr\cos\theta} P_l(\cos\theta) d\theta = \sum_{n=0}^{\infty} A_n J_n(kr) \int_0^{\pi} P_n(\cos\theta) P_l(\cos\theta) d\theta$$

Let $x = \cos\theta$ so that $dx = -\sin\theta d\theta$ then $d\theta = -\frac{dx}{\sin\theta}$ , so the integral takes the following form

$$\int_{-1}^{1} e^{ikrx} P_l(x) dx = \sum_{n=0}^{\infty} A_n J_n(kr) \int_{-1}^{1} P_n(x) P_l(x) dx \tag{2.5}$$

Note that in this last expression, we can make use of the orthogonality property of Legendre polynomials, which establishes that

$$\int_{-1}^{1} P_n(x)P_l(x)dx = \frac{2}{2n+1}\delta_{nl}$$

for $n = l$, substituting this property in equation (2.5), we obtain

$$\int_{-1}^{1} e^{ikrx}P_l(x)dx = \sum_{n=0}^{\infty} A_n J_n(kr)\frac{2}{2n+1}\delta_{nl} \tag{2.6}$$

As we can see in equation (2.3), we have two cases for the Kronecker delta

- First case: if $n = l$ then $\delta = 1$
- Second case: if $n \neq l$ then $\delta = 0$

For the following development, it is necessary to start from the first case of the Kronecker delta, then

$$\int_{-1}^{1} e^{ikrx}P_l(x)dx = \sum_{l=0}^{\infty} A_l J_l(kr)\frac{2}{2l+1} \tag{2.7}$$

Integrating by parts the left hand side of equation (2.7) gives

$$\int_{-1}^{1} e^{ikrx}P_x dx = \frac{1}{ikr}\left[e^{ikr}P_l(1) - e^{-ikr}P_l(-1)\right] - \int_{-1}^{1} P_l'(x)\frac{e^{ikrx}}{ikr}dx$$

$$= \frac{1}{ikr}\left[e^{ikr}P_l(1) - e^{-ikr}P_l(-1)\right] - \frac{1}{(ikr)^2}\left[e^{ikr}P_l'(1) - e^{-ikr}P_l'(-1)\right] + \dots$$

And making use of the asymptotic approximation in the second term of the right side of the equality we have that this tends to zero, so the integral is equal to

$$\int_{-1}^{1} e^{ikrx}P_l(x)dx = \frac{1}{ikr}\left[e^{ikr}P_l(1) - e^{-ikr}P_l(-1)\right]$$

Remembering that $P_l(1) = 1$ and $P_l(-1) = (-1)^l = e^{i\pi l}$ ,

$$\int_{-1}^{1} e^{ikrx}P_l(x)dx = \frac{1}{ikr}\left[e^{ikr} - e^{-ikr}(-1)^l\right]$$

$$= \frac{1}{ikr}\left[e^{ikr} - e^{-ikr}e^{i\pi l}\right]$$

Thus equation (2.4) can be expressed as

$$\frac{1}{ikr}\left[e^{ikr} - e^{-ikr}e^{i\pi l}\right] = \sum_{l=0}^{\infty} A_l J_l(kr)\frac{2}{2l+1}$$

Substituting the spherical Bessel function in the previous expression

$$\frac{1}{ikr}\left[e^{ikr} - e^{-ikr}e^{i\pi l}\right] = \sum_{l=0}^{\infty} A_l \left[\frac{1}{kr}\sin\left(kr - \frac{l}{2}\pi\right)\right]\frac{2}{2l+1}$$

$$= \frac{1}{kr}\sum_{l=0}^{\infty} A_l \sin\left(kr - \frac{l}{2}\pi\right)\frac{2}{2l+1}$$

Multiplying both sides of the equality by $e^{i\pi\frac{l}{2}}$

$$\frac{e^{i\pi\frac{l}{2}}}{ikr}\left[e^{ikr} - e^{-ikr}e^{i\pi l}\right] = \frac{1}{kr}\sum_{l=0}^{\infty} e^{i\pi\frac{l}{2}} A_l \sin\left(kr - \frac{l}{2}\pi\right)\frac{2}{2l+1}$$

$$\implies \frac{e^{i\pi\frac{l}{2}}}{ikr}\left[e^{ikr - i\pi\frac{l}{2}} - e^{-ikr + i\pi\frac{l}{2}}\right] = \frac{1}{kr}\sum_{l=0}^{\infty} A_l \sin\left(kr - \frac{l}{2}\pi\right)\frac{2}{2l+1}$$

$$\implies \frac{e^{i\pi\frac{l}{2}}}{i}\left[e^{i(kr - \pi\frac{l}{2})} - e^{-i(kr - \pi\frac{l}{2})}\right] = \sum_{l=0}^{\infty} A_l \sin\left(kr - \frac{l}{2}\pi\right)\frac{2}{2l+1}$$

$$\implies 2e^{i\pi\frac{l}{2}}\left[\frac{e^{i(kr - \pi\frac{l}{2})} - e^{-i(kr - \pi\frac{l}{2})}}{2i}\right] = \sum_{l=0}^{\infty} A_l \sin\left(kr - \frac{l}{2}\pi\right)\frac{2}{2l+1}$$

Making use of the $\sin x = \frac{e^{ix} - e^{-ix}}{2i}$ property, we have

$$2e^{i\pi\frac{l}{2}}\sin\left(kr - \pi\frac{l}{2}\right) = \sum_{l=0}^{\infty} A_l \sin\left(kr - \frac{l}{2}\pi\right)\frac{2}{2l+1}$$

$$\implies 2e^{i\pi\frac{l}{2}} = \sum_{l=0}^{\infty} A_l \frac{2}{2l+1}$$

We proceed to clear the normalization factor

$$A_l = (2l+1)e^{i\pi\frac{l}{2}}$$

Note that

$$e^{i\pi\frac{l}{2}} = \left(e^{i\frac{\pi}{2}}\right)^l = \left(\cos\left(\frac{\pi}{2}\right) + i\sin\left(\frac{\pi}{2}\right)\right)^l = i^l$$

Thus the normalization factor is given by

$$A_l = (2l+1)i^l$$

Since we know the normalization factor it is possible to write to the total wave function at long distances as

$$\psi = \psi_{inc} + \psi_{scatt} = e^{ikr\cos\theta} + f(\theta,\phi)\frac{e^{ikr}}{r}$$

$$= \sum_{l=0}^{\infty} A_l J_l(kr) P_l(\cos\theta) + f(\theta,\phi)\frac{e^{ikr}}{r}$$

$$= \sum_{l=0}^{\infty}(2l+1)i^l J_l(kr) P_l(\cos\theta) + f(\theta,\phi)\frac{e^{ikr}}{r}$$

$$= \frac{1}{kr}\sum_{l=0}^{\infty}(2l+1)i^l \sin\left(kr - \frac{l}{2}\pi\right) P_l(\cos\theta) + f(\theta,\phi)\frac{e^{ikr}}{r}$$

$$= \frac{1}{kr}\sum_{l=0}^{\infty}(2l+1)i^l \left(\frac{e^{ikr}(-i)^l - e^{-ikr}i^l}{2i}\right) P_l(\cos\theta) + f(\theta,\phi)\frac{e^{ikr}}{r} \tag{2.8}$$

**Phase shifts**

We proceed to calculate the total wave function, for this we have to solve the Schrödinger equation independent of time

$$\left(-\frac{\hbar^2}{2m}\nabla^2 + V(r)\right)\psi = E\psi \tag{2.9}$$

Where $\psi$ is given by

$$\psi = \sum_{l=0}^{\infty} R(r) Y_l^m(\theta,\phi)$$

On the other hand, let us remember that the Laplacian in spherical coordinates is

$$\nabla^2 = \frac{1}{r^2}\frac{\partial}{\partial r}\left(r^2\frac{\partial}{\partial r}\right) + \frac{1}{r^2\sin\theta}\frac{\partial}{\partial\theta}\left(\sin\theta\frac{\partial}{\partial\theta}\right) + \frac{1}{r^2\sin^2\theta}\frac{\partial^2}{\partial\phi^2}$$

Now, let's consider a specific value of $l$ and introducing the wave function and the Laplacian in equation (2.9) we have

$$\left(-\frac{\hbar^2}{2m}\nabla^2 + V(r)\right) R(r)Y_l^m(\theta,\phi) = ER(r)Y_l^m(\theta,\phi)$$

$$\begin{aligned}
\implies \left[-\frac{\hbar^2}{2m}\left(\frac{1}{r^2}\frac{\partial}{\partial r}\left(r^2\frac{\partial}{\partial r}\right) + \frac{1}{r^2\sin\theta}\frac{\partial}{\partial\theta}\left(\sin\theta\frac{\partial}{\partial\theta}\right) + \frac{1}{r^2\sin^2\theta}\frac{\partial^2}{\partial\phi^2}\right) + V(r)\right] R(r)Y_l^m(\theta,\phi) \\
= ER(r)Y_l^m(\theta,\phi) \\
\implies -\frac{\hbar^2}{2m}\left(\frac{1}{r^2}\frac{\partial}{\partial r}\left(r^2\frac{\partial}{\partial r}\right)\right) R(r)Y_l^m(\theta,\phi) \\
-\frac{\hbar^2}{2m}\left[\frac{1}{r^2\sin\theta}\frac{\partial}{\partial\theta}\left(\sin\theta\frac{\partial}{\partial\theta}\right) + \frac{1}{r^2\sin^2\theta}\frac{\partial^2}{\partial\phi^2}\right] R(r)Y_l^m(\theta,\phi) \\
+V(r)R(r)Y_l^m(\theta,\phi) = ER(r)Y_l^m(\theta,\phi) \qquad (2.10)
\end{aligned}$$

From this last expression we can simplify the angular part, we know that the square of the angular momentum in spherical angular coordinates is

$$L^2 = -\hbar^2\left(\frac{1}{\sin\theta}\frac{\partial}{\partial\theta}\left(\sin\theta\frac{\partial}{\partial\theta}\right) + \frac{1}{\sin^2\theta}\frac{\partial^2}{\partial\phi^2}\right)$$

Previously we have mentioned that the functions $Y_l^m$ are called spherical harmonics, of which the eigenvalue is

$$L^2Y_l^m = l(l+1)\hbar^2Y_l^m$$

Which we substitute in the equation (2.10)

$$\begin{aligned}
-\frac{\hbar^2}{2m}\left(\frac{1}{r^2}\frac{\partial}{\partial r}\left(r^2\frac{\partial}{\partial r}\right)\right) R(r)Y_l^m(\theta,\phi) - \frac{\hbar^4}{2mr^2}l(l+1)R(r)Y_l^m(\theta,\phi) + V(r)R(r)Y_l^m(\theta,\phi) \\
= ER(r)Y_l^m(\theta,\phi) \\
\implies -\frac{\hbar^2}{2m}\left(\frac{1}{r^2}\frac{\partial}{\partial r}\left(r^2\frac{\partial}{\partial r}\right)\right) R(r) - \frac{\hbar^4}{2mr^2}l(l+1)R(r) + (V(r)-E)\,R(r) = 0 \\
\implies -\frac{\hbar^2}{2m}\left(\frac{1}{r^2}\frac{\partial}{\partial r}\left(r^2\frac{\partial}{\partial r}\right)\right) R(r) + \left[(V(r)-E) - \frac{\hbar^4}{2mr^2}l(l+1)\right] R(r) = 0 \qquad (2.11)
\end{aligned}$$

Now, we make the following variable change

$$u(r) = rR(r)$$

So that the Radial part can be expressed as

$$R(r) = \frac{u(r)}{r} \Longrightarrow R = \frac{u}{r}$$

This last relation allows us to calculate the terms related to the radial part of equation (2.8).

$$\frac{\partial R}{\partial r} = \frac{\partial}{\partial r}\left(\frac{u}{r}\right) = \frac{r\left(\frac{\partial u}{\partial r}\right) - u}{r^2} = \frac{1}{r}\frac{\partial u}{\partial r} - \frac{u}{r^2}$$

$$\Longrightarrow r^2\left(\frac{\partial R}{\partial r}\right) = r^2\left(\frac{1}{r}\frac{\partial u}{\partial r} - \frac{u}{r^2}\right) = r\frac{\partial u}{\partial r} - u$$

$$\Longrightarrow \frac{\partial}{\partial r}\left[r^2\left(\frac{\partial R}{\partial r}\right)\right] = \frac{\partial}{\partial r}\left[r\frac{\partial u}{\partial r} - u\right] = \frac{\partial}{\partial r}\left(r\frac{\partial u}{\partial r}\right) - \frac{\partial u}{\partial r}$$

$$= \frac{\partial u}{\partial r} + r\frac{\partial^2 u}{\partial r^2} - \frac{\partial u}{\partial r} = r\frac{\partial^2 u}{\partial r^2}$$

We proceed to substitute the calculated terms in equation (2.11)

$$-\frac{\hbar^2}{2mr}\left(\frac{\partial^2 u}{\partial r^2}\right) + \left[(V(r) - E) - \frac{\hbar^4}{2mr^2}l(l+1)\right]\frac{u}{r} = 0$$

$$\Longrightarrow \frac{1}{r}\left[-\frac{\hbar^2}{2m}\left(\frac{\partial^2 u}{\partial r^2}\right) + \left[(V(r) - E) - \frac{\hbar^4}{2mr^2}l(l+1)\right]u\right] = 0$$

$$-\frac{\hbar^2}{2m}\left(\frac{\partial^2 u}{\partial r^2}\right) + \left[(V(r) - E) - \frac{\hbar^4}{2mr^2}l(l+1)\right]u = 0 \tag{2.12}$$

Now, let $V(r) = 0$

$$-\frac{\hbar^2}{2m}\left(\frac{\partial^2 u}{\partial r^2}\right) + \left[E - \frac{\hbar^4}{2mr^2}l(l+1)\right]u = 0$$

Note that the above expression is similar to Bessel's equation, so that the solution to

this differential equation is given by

$$u = AJ_l(kr) + Bn_l(kr)$$

Where A and B are constants. And from the asymptotic behavior it follows that

$$J_l(kr) = \frac{1}{kr}\sin\left(kr - \frac{l}{2}\pi\right)$$

$$n_l(kr) = \frac{1}{kr}\sin\left(kr - \frac{(l+1)}{2}\pi\right)$$

Substituting in the radial function

$$R(r) = \frac{u(r)}{r} = \frac{1}{r}\left[AJ_l(kr) + Bn_l(kr)\right] = \frac{A}{r}J_l(kr) + \frac{B}{r}n_l(kr)$$

$$= \frac{A}{r}\left[\frac{1}{kr}\sin\left(kr - \frac{l}{2}\pi\right)\right] + \frac{B}{r}\left[\frac{1}{kr}\sin\left(kr - \frac{(l+1)}{2}\pi\right)\right]$$

And substituting $A_0 = \frac{A}{r}$ and $B_0 = \frac{B}{r}$, we obtain

$$R(r) = A_0\left[\frac{1}{kr}\sin\left(kr - \frac{l}{2}\pi\right)\right] + B_0\left[\frac{1}{kr}\sin\left(kr - \frac{(l+1)}{2}\pi\right)\right]$$

We introduce the phase shift $A_0 = A_l\cos\delta$ and $B_0 = -A_l\sin\delta$

$$R(r) = \frac{1}{kr}\left[A_l\cos\delta\sin\left(kr - \frac{l}{2}\pi\right) - A_l\sin\delta\sin\left(kr - \frac{(l+1)}{2}\pi\right)\right]$$

$$= \frac{A_l}{kr}\left[\cos\delta\sin\left(kr - \frac{l}{2}\pi\right) - \sin\delta\sin\left(kr - \frac{(l+1)}{2}\pi\right)\right] \tag{2.13}$$

On the other hand

$$\sin\left(kr - \frac{(l+1)}{2}\pi\right) = \sin\left(kr - \frac{l}{2}\pi - \frac{\pi}{2}\right) = -\sin\left(\frac{\pi}{2} - \left(kr - \frac{l}{2}\pi\right)\right)$$

$$= -\left[\sin\left(\frac{\pi}{2}\right)\cos\left(kr - \frac{l}{2}\pi\right) - \sin\left(kr - \frac{l}{2}\pi\right)\cos\left(\frac{\pi}{2}\right)\right] = -\cos\left(kr - \frac{l}{2}\pi\right)$$

We substitute the above in equation (2.13)

$$R(r) = \frac{A_l}{kr}\left[\cos\delta \sin\left(kr - \frac{l}{2}\pi\right) + \sin\delta\cos\left(kr - \frac{l}{2}\pi\right)\right]$$

$$\implies R(r) = \frac{A_l}{kr}\sin\left(\delta + kr - \frac{l}{2}\pi\right)$$

Thus we have that the incident wave function is

$$\psi_{inc} = \sum_{l=0}^{\infty} R(r) Y_l^m(\theta,\phi)$$

$$= \sum_{l=0}^{\infty} \frac{A_l}{kr}\sin\left(\delta + kr - \frac{l}{2}\pi\right) Y_l^m(\theta,\phi)$$

$$= \frac{1}{kr}\sum_{l=0}^{\infty}(2l+1)i^l \sin\left(\delta + kr - \frac{l}{2}\pi\right) P_l(\cos\theta)$$

Where $A_l = (2l+1)i_l$ and $Y_l^m(\theta,\phi) = P_l(\cos\theta)$. Therefore, the total wave function is

$$\psi_{inc} = \frac{1}{kr}\sum_{l=0}^{\infty}(2l+1)i^l \sin\left(\delta + kr - \frac{l}{2}\pi\right) P_l(\cos\theta) + f(\theta,\phi)\frac{e^{ikr}}{r}$$

$$= \frac{1}{kr}\sum_{l=0}^{\infty}(2l+1)i^l \left(\frac{e^{i\left(\delta+kr-\frac{l}{2}\pi\right)} - e^{-i\left(\delta+kr-\frac{l}{2}\pi\right)}}{2i}\right) P_l(\cos\theta) + f(\theta,\phi)\frac{e^{ikr}}{r} \tag{2.14}$$

Note that

$$e^{\pm i\frac{l}{2}\pi} = \left(\pm e^{i\frac{\pi}{2}}\right)^l = \pm\left(\cos\left(\frac{\pi}{2}\right) + i\sin\left(\frac{\pi}{2}\right)\right)^l = \pm i^l$$

Knowing this, we can write the total wave function as follows

$$\psi_{total} = \frac{1}{kr}\sum_{l=0}^{\infty}(2l+1)i^l \left(\frac{(-i)^l e^{i(\delta+kr)} - (i)^l e^{-i(\delta+kr)}}{2i}\right) P_l(\cos\theta) + f(\theta,\phi)\frac{e^{ikr}}{r}$$

$$= \frac{1}{2ikr}\sum_{l=0}^{\infty}(2l+1)i^l \left((-i)^l e^{i(\delta+kr)} - (i)^l e^{-i(\delta+kr)}\right) P_l(\cos\theta) + f(\theta,\phi)\frac{e^{ikr}}{r}$$

On the one hand, the incident wave function can be developed as follows

$$\psi_{inc} = -\frac{e^{-ikr}}{2ikr}\sum_{l=0}^{\infty}(2l+1)i^{2l}e^{-i\delta}P_l(\cos\theta) + \frac{e^{ikr}}{2ikr}\sum_{l=0}^{\infty}(2l+1)(i^l)(-i^l)e^{i\delta}P_l(\cos\theta)$$

$$= -\frac{e^{-ikr}}{2ikr}\sum_{l=0}^{\infty} A_l i^l e^{-i\delta} P_l(\cos\theta) + \frac{e^{ikr}}{2ikr}\sum_{l=0}^{\infty} A_l(-i^l)e^{i\delta}P_l(\cos\theta) \tag{2.15}$$

We take from equation (2.8) the expression corresponding to the incident wave function and we develop it

$$\psi_{inc} = \frac{1}{2ikr}\sum_{l=0}^{\infty}(2l+1)i^l\left((-i^l)e^{ikr} - i^l e^{-ikr}\right)P_l(\cos\theta)$$

$$= -\frac{e^{-ikr}}{2ikr}\sum_{l=0}^{\infty}(2l+1)i^{2l}P_l(\cos\theta) + \frac{e^{ikr}}{2ikr}\sum_{l=0}^{\infty}(2l+1)(i^l)(-i^l)P_l(\cos\theta)$$

We can see that this last expression has a similar form to equation (2.15), so we proceed to compare them and obtain the following result

$$(2l+1)i^{2l} = A_l i^l e^{-i\delta}$$

$$\Longrightarrow A_l = (2l+1)i^l e^{i\delta} \tag{2.16}$$

We substitute equation (2.16) into equation (2.15) to obtain the incident wave function

$$\psi_{inc} = -\frac{e^{-ikr}}{2ikr}\sum_{l=0}^{\infty}(2l+1)i^l e^{i\delta} i^l e^{-i\delta}P_l(\cos\theta) + \frac{e^{ikr}}{2ikr}\sum_{l=0}^{\infty}(2l+1)i^l e^{i\delta}(-i^l)e^{i\delta}P_l(\cos\theta)$$

$$= -\frac{e^{-ikr}}{2ikr}\sum_{l=0}^{\infty}(2l+1)i^{2l}P_l(\cos\theta) + \frac{e^{ikr}}{2ikr}\sum_{l=0}^{\infty}(2l+1)i^l(-i^l)e^{i2\delta}P_l(\cos\theta) \tag{2.17}$$

Thus we obtain the total wave function

$$\psi_{total} = -\frac{e^{-ikr}}{2ikr}\sum_{l=0}^{\infty}(2l+1)i^{2l}P_l(\cos\theta) + \frac{e^{ikr}}{2ikr}\sum_{l=0}^{\infty}(2l+1)i^l(-i^l)e^{i2\delta}P_l(\cos\theta) + f(\theta,\phi)\frac{e^{ikr}}{r}$$

$$= -\frac{e^{-ikr}}{2ikr}\sum_{l=0}^{\infty}(2l+1)i^{2l}P_l(\cos\theta) + \frac{e^{ikr}}{r}\left[\frac{1}{2ik}\sum_{l=0}^{\infty}(2l+1)i^l(-i^l)e^{i2\delta}P_l(\cos\theta) + f(\theta,\phi)\right]$$

On the other hand, we equal the terms of the equations (2.17) and (2.8) that contain the coefficient $\frac{e^{ikr}}{r}$

$$\Longrightarrow \frac{e^{ikr}}{r}\left[\frac{1}{2ik}\sum_{l=0}^{\infty}(2l+1)i^l(-i^l)P_l(\cos\theta) + f(\theta,\phi)\right] = \frac{e^{ikr}}{r}\left[\frac{1}{2ik}\sum_{l=0}^{\infty}(2l+1)i^l(-i^l)e^{i2\delta}P_l(\cos\theta)\right]$$

$$\implies f(\theta,\phi)+\frac{1}{2ik}\sum_{l=0}^{\infty}(2l+1)i^l(-i^l)P_l(\cos\theta)=\frac{1}{2ik}\sum_{l=0}^{\infty}(2l+1)i^l(-i^l)e^{i2\delta}P_l(\cos\theta)$$

We clear the scattering amplitude

$$f(\theta,\phi)=\frac{1}{2ik}\sum_{l=0}^{\infty}(2l+1)i^l(-i^l)P_l(\cos\theta)(e^{i2\delta}-1)$$

Note that

$$\frac{e^{2i\delta}}{2i}=e^{i\delta}\sin\delta$$

and

$$i^l(-i^l)=1$$

So the scattering amplitude is in terms of the phase shifts as shown in the following expression.

$$f(\theta,\phi)=\frac{1}{k}\sum_{l=0}^{\infty}(2l+1)e^{i\delta}\sin\delta P_l(\cos\theta)$$

**The total cross-section**

The cross-section can be expressed in terms of the scattering amplitude, as well as in a sum over the angular momentum of the partial cross-sections. Thus we have that the differential cross-section is given by

$$\frac{\partial\sigma_l}{\partial\Omega}=\mid f(\theta,\phi)\mid^2=\left|\frac{1}{k}\sum_{l=0}^{\infty}(2l+1)e^{i\delta}\sin\delta P_l(\cos\theta)\right|^2$$

$$=\frac{1}{k^2}\left|\sum_{l=0}^{\infty}(2l+1)e^{i\delta}\sin\delta P_l(\cos\theta)\right|^2$$

Thus the total cross-section is

$$\sigma=\int\frac{\partial\sigma_l}{\partial\Omega}d\Omega=\int_0^{\pi}\int_0^{2\pi}\frac{\partial\sigma}{\partial\Omega}\sin\theta d\theta d\phi=\int_0^{\pi}|f(\theta)|^2\sin\theta d\theta\int_0^{2\pi}d\phi$$

$$=2\pi\int_0^{\pi}|f(\theta)|^2\sin\theta d\theta$$

Note that

$$|f(\theta)|^2 = \frac{1}{k^2}\sum_{l=0}^{\infty}\sum_{l'=0}^{\infty}(2l+1)(2l'+1)e^{i(\delta-\delta')}\sin\delta\sin\delta' P_l(\cos\theta)P_{l'}(\cos\theta)$$

Therefore, the total cross-section is given by

$$\sigma = \frac{2\pi}{k^2}\sum_{l=0}^{\infty}\sum_{l'=0}^{\infty}(2l+1)(2l'+1)e^{i(\delta-\delta')}\sin\delta\sin\delta'\int_0^{\pi}P_l(\cos\theta)P_{l'}(\cos\theta)\sin\theta d\theta \quad (2.18)$$

Using the following expression

$$\int_0^{\pi}P_l(\cos\theta)P_{l'}(\cos\theta)\sin\theta d\theta = \frac{2}{2l+1}\delta_{ll'}$$

and substituting the above expression in the equation (2.18) and considering $l = l'$, we have

$$\sigma = \frac{2\pi}{k^2}\sum_{l=0}^{\infty}(2l+1)^2\sin^2\delta\left(\frac{2}{2l+1}\right) = \frac{4\pi}{k^2}\sum_{l=0}^{\infty}(2l+1)\sin^2\delta$$

Thus

$$\sigma = \frac{4\pi}{k^2}\sum_{l=0}^{\infty}(2l+1)\sin^2\delta \quad (2.19)$$

**Optical Theorem**

The optical theorem within wave scattering theory establishes a relationship between the imaginary part of the scattering amplitude with the total cross section. "The theorem follows from very general considerations of the conservation of energy and power flow, and has its counterpart in the quantum-mechanical scattering of particles through the conservation of probability" [14]. For establishing this theorem, we consider the scattering amplitude

$$f(\theta,\phi) = \frac{1}{k}\sum_{l=0}^{\infty}(2l+1)e^{i\delta}\sin\delta P_l(\cos\theta)$$

We must consider that $\theta = 0$ , so that, $P_l(\cos\theta) = P_l(1) = 1$ so we can write the

scattering amplitude as

$$f(\theta,\phi) = \frac{1}{k}\sum_{l=0}^{\infty}(2l+1)e^{i\delta}\sin\delta = \frac{1}{k}\sum_{l=0}^{\infty}(2l+1)\left(\cos\delta + i\sin\delta\right)\sin\delta$$

$$= \frac{1}{k}\sum_{l=0}^{\infty}(2l+1)\left(\cos\delta\sin\delta + i\sin^2\delta\right)$$

Taking the imaginary part

$$f(\theta,\phi) = \frac{1}{k}\sum_{l=0}^{\infty}(2l+1)\sin^2\delta$$

It should be noted that the cross-section can be related to the dispersion amplitude as follows

$$\sigma = \frac{4\pi}{k^2}\sum_{l=0}^{\infty}(2l+1)\sin^2\delta$$

$$= \frac{4\pi}{k}[Im(f(\theta,\phi)]$$

This last equation describes the optical theorem.

## 2.4 Collins-Soper frame of reference

There are different reference frames used to analyze particle decays, in this section we focus on the study of the Collins-Soper (CS) reference frame [16], for this, we consider the angular distribution of a pair of particles produced in high energy hadron collisions. The CS reference frame is measured in the rest frame of the resulting particle, so, from the experimental perspective, a double Lorentz transformation from the laboratory system to CS frame is needed.

From the classical point of view, we must apply a Lorentz boost from the laboratory frame to the center of mass of the particle we are interested to study, "followed by a pure rotation such that the new $z$ axis forms equal angles with the initial-state beams/partons" [18]. Another way to move from the laboratory frame to the CS system is to employ two consecutive boosts, first a longitudinal boost, which brings

the particle into the system where its momentum in the z-component is zero $p_z = 0$, followed by a transverse boost to the center of mass where the transverse momentum of the particle is equal to the total transverse momentum, which is equal to zero.

Let us consider the central process $p_a + p_b \longrightarrow p_1 + X + p_2$ where $X \equiv X_3 + X_4$ refers to a pair of particles. We can assume that the 4-momentum is composed of the energy and each of the projections of the tri-momentum vector onto the $x$, $y$ and $z$ axes. Establish the matrix transformation that takes us from the laboratory system to the Collins-Soper frame of reference as follows:

$$\Lambda\left(LAB \longrightarrow CS\right) = \begin{pmatrix} r_E & -r & 0 & -r_z \\ -\frac{r_E r}{\sqrt{1+r^2}} & \sqrt{1+r^2} & 0 & \frac{r_z r}{\sqrt{1+r^2}} \\ 0 & 0 & 1 & 0 \\ -\frac{r_z}{\sqrt{1+r^2}} & 0 & 0 & \frac{r_E}{\sqrt{1+r^2}} \end{pmatrix} \tag{2.20}$$

Where $r_E \equiv \frac{E^X}{M}$, $r_z \equiv \frac{p_z^X}{M}$ and $r \equiv \frac{p_T}{M}$ [18]. From this notation, it must be specified that $p_z^X$ denotes the longitudinal momentum of the pair of particles, while $p_T$ and $M$ are the transverse momentum and mass of the system X.

Note that this reaction leads us to establish the axes of the CS system from a set of unit vectors

$$e_3 = \frac{\hat{p_a} - \hat{p_b}}{|\ \hat{p_a} - \hat{p_b}\ |}$$

$$e_2 = \frac{\hat{p_a} \times \hat{p_b}}{|\ \hat{p_a} \times \hat{p_b}\ |}$$

$$e_1 = \frac{\hat{p_a} + \hat{p_b}}{|\ \hat{p_a} + \hat{p_b}\ |}$$

"This satisfy the condition $e_1 = e_2 \times e_3$. Here $\hat{p_a} = \frac{p_a}{|p_a|}$, $\hat{p_b} = \frac{p_b}{|p_b|}$, where $p_a$, $p_b$ are the three-momenta of the initial protons in the $\pi^+\pi^-$ rest system. There we have $p_{34} = 0$ and $p_a + p_b = p_1 + p_2$" [16].

Now that the axes are established, we set the polar angle for the $X_3$ particle relative

to the axes, i.e.

$$\cos\theta_{x_3} = \hat{p_3} \cdot e_3$$

In Fig. 2.3 an illustration of the Collins-Soper frame is shown.

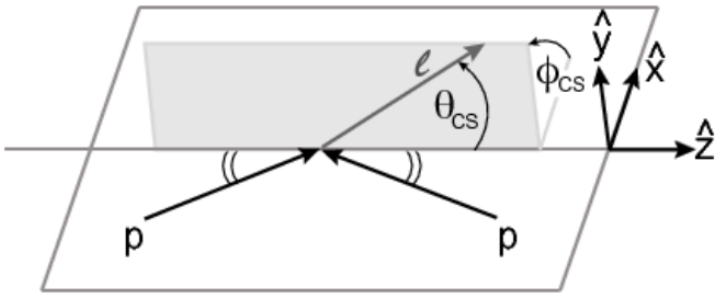


Figure 2.3: Collins-Soper framework reference diagram [3]

## 2.5 Regge Theory

The Regge theory emerged in 1959 when Regge demonstrated that in order to solve the Schrödinger equation for a non-relativistic scattering potential it is necessary to consider the angular momentum as a complex variable. Regge proved that for a vast set of potentials there are unique singularities related to the scattering amplitude which he called "poles", these poles are located in the complex plane and can take positive values for the angular momentum which correspond to resonances or bound states.

From the perspective of quantum mechanics, "the bound states for spherically symmetric potential fall into families with increasing angular momentum and energy. These bound states appear as poles of the partial wave amplitude with a given integer angular momentum" [17]. It is important to point out that these poles in the presence of a well-behaved potential are located in a straight line, which is known as Regge trajectory, and is represented as follows

$$\alpha_R(t) = \alpha_R(0) + \alpha_R^{'}(0)t$$

"Where $\alpha_R(0)$ is called the intercept and $\alpha_R^{'}(0)$ the slope" [17], at this point it is

convenient to establish that the Pomeron is related to the increase of the cross section as the collision energy increases, in addition to this, it is also considered as one of the trajectories of the present theory, which has an intercept value of $\alpha_R(0) = 1.08$ and a slope of $\alpha'_R(0) = 0.25 GeV^{-2}$. In Fig. 2.4 some Regge trajectories are shown.

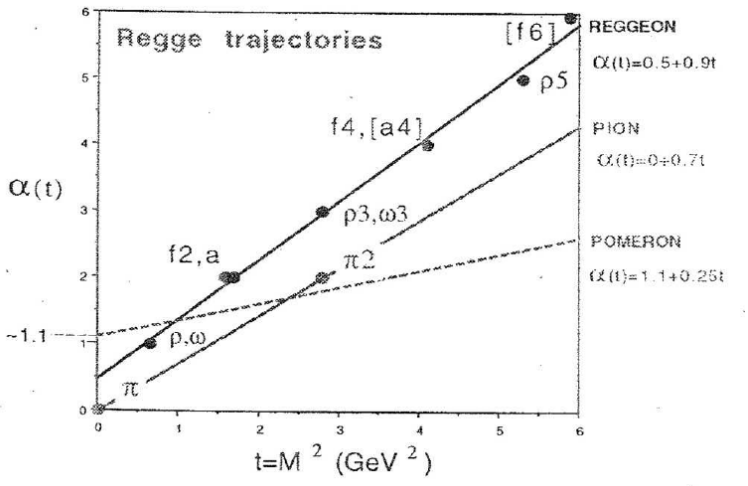


Figure 2.4: Regge Trajectories [17]

## 2.6 Resonances

A resonance usually refers short-lived particles, that exhibits a peak originated at a specific energy related directly with the cross section. On the other hand, it is relatively easy to know their energies, since it is enough to observe the maxima or peaks of the cross sections.

Particle physics points out that after a collision, the particle formed during the process can decay instantaneously into more stable particles and, taking up the definition of resonance, it is possible to say that "the energy is a resonant state of the reaction between the colliding particles, an energy at which the collision is more probable" [11].

### 2.6.1 Glueballs

Within the theory of Quantum Chromodynamics or by its acronym QCD, a particle that acts as a carrier of the strong nuclear interaction, which is characterized by being a

boson and having a color charge, is called a gluon. These particles have the particularity of being able to interact and couple with other gluons or quarks, therefore, it is possible that between them they form bound states of gluons, known as Glueballs.

The glueballs have the peculiarity of not having radiative decay but they usually decay to a pair of pseudoscalars, such as $\pi^+\pi^-$, $K^+K^-$, $\eta\eta$ , among others. The predicted mass of the glueballs is in the range of $1-2$ GeV [22].

## 2.7 ALICE experiment

A Large Ion Collider Experiment or ALICE is one of the four main detectors of the Large Hadron Collider (LHC), it is devoted to the study of matter known as quark-gluon plasma (QGP). ALICE, measuring $16\times16\times26m^3$ and with a mass of ten thousand tons, located 56 meters underground on the French-Swiss border, it has a collaboration of approximately 2000 scientists from 174 physics institutes in 40 countries around the world [1].

The reference system of this detector is based on the Cartesian coordinate system, whose origin (0,0,0) is located at the center of the central barrel of ALICE, based on this, it is established that the $x$ axis points to the center of the LHC ring, the $y$ axis is orthogonal to the $xz$ plane and the $z$ axis is along the beam line. It is important to note, that this experiment has an excellent particle identification system (PID) and "was designed to operate at very high multiplicity environment" [24], which occurs in collisions between heavy ions.

The central barrel of the ALICE experiment consists of 7 subsystems or detectors: ITS, TPC, TRD, TOF, PHOS, EMCal and HMPID, in addition to these it has a Muon Spectrometer, located inside a solenoid magnet capable to generate a $B = 0.5$T, which is parallel to the beam axis, whose function is to deflect the trajectory of the particles. On the other hand, at the front and back of the barrel, the detectors PMD, FMD, V0,T0,ZDC and AD are located.

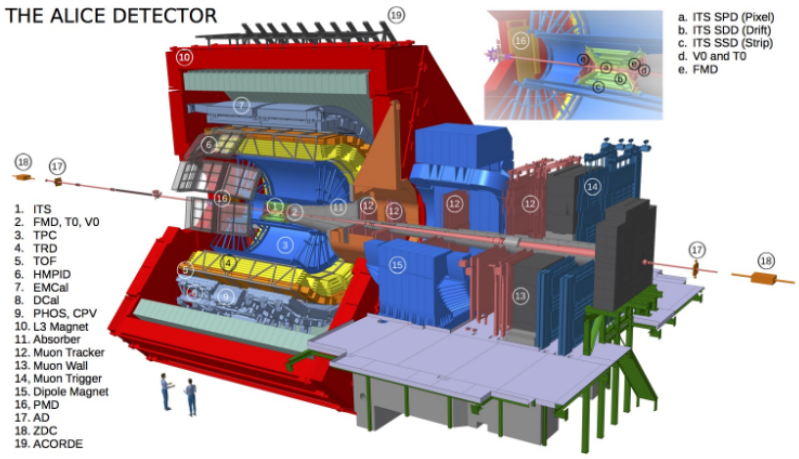


Figure 2.5: ALICE experiment [24]

### 2.7.1 The Time Projection Chamber (TPC)

"The Time Projection Chamber is the main detector of ALICE, used for tracking and particle identification" [24], is a gas detector composed of a Ne-CO2-N2 (90-10-5) mixture [2], with a cylindrical shape of approximately $90m^3$. The TPC has a pseudorapidity of $|\eta| < 0.9$ and an acceptability along the azimuthal angle of $2\pi$. On the other hand, the identification of charged particles is carried out from their energy deposition, which is parameterized by the Bethe-Bloch equation.

### 2.7.2 The Inner Tracking System (ITS)

The Inner Tracking System, or ITS for its initials, this "is the nearest detector to the interaction point , roughly 4 cm for the innermost layer, and 43 cm for the outermost" [24]. The purpose of ITS is the determination and reconstruction of the primary and secondary vertex, respectively, as well as the tracking and identification of low momenta particles. The ITS is composed of three subsystems: the SPD, SDD and SSD, which have concentric silicon detectors.

The SPD constitutes the first two layers of the ITS, this detector reconstructs the secondary vertices. The next two layers (or intermediate layers of the ITS) are the SDD detector and the two outermost layers of the detector correspond to the SSD

whose objective is to align the trajectories obtained by the TPC and the ITS.

### 2.7.3 The Transition Radiation Detector (TRD)

It is a detector that focuses on electron identification and together with the TPC and ITS provides the necessary information for the analysis and study of light and heavy mesons, it is worth noting that the TRD is composed of 522 detectors and "it has 1.15 million of channels of readout, each sampling the signal in 20 time bins. The active gas is a xenon-CO2 mixture" [2].

### 2.7.4 The Time of Flight (TOF)

This detector is composed of Multigap Resistive Plate Chambers or by its acronym (MRPCs), its function is based on the identification of charged particles whose momentum is of an intermediate range and works as a trigger for events coming from ultraperipheral collisions and cosmic rays. The TOF has a high precision to measure the time of flight of each particle, from which it makes the identification of the species to which they correspond.

### 2.7.5 The Forward Detectors

Previously, it was mentioned that ALICE has a set of detectors covering the regions of acceptability in the front and back of the central barrel, they are used as a trigger for minimum bias and diffractives events, among others, and to determine the event reaction plane and centrality of the heavy-ion collisions.

The V0 detector aims to generate a fast level-0 trigger signal for minimum bias events. It is used for event reaction plane and centrality determination in heavy-ion collisions. This detector consists of two sets of plastic scintillator V0A and V0C located at 3.29 meters and 5.90 meters from the interaction point of ALICE.

The AD detector or ALICE Diffractive Detector, aims to increase the pseudorapidity of

the ALICE experiment, to contribute to the improvement of the minimum bias trigger and selection of diffractive events in proton-proton collisions.

## 2.8 Partial Wave Analysis in ALICE at $\sqrt{s} = 7TeV$

During Run 1 of the ALICE experiment, the central production of the pion pair ($\pi^+\pi^-$) in proton-proton collisions with center-of-mass energies of 7 TeV was studied from the application of the double gap. Consequently, partial wave analysis was implemented on the experimental sample, with the aim of studying the properties and the differential cross section of the $\pi^+\pi^-$ system, based on the $f_0(980)$ and $f_2(1270)$ resonances.

### 2.8.1 Experimental development of Partial Wave Analysis

The implementation of partial wave analysis for the decay of two pseudoscalars in the final state begins with the translation of the Laboratory reference frame to the Collins-Soper (CS) or Gottfried-Jackson (GJ) frame, where both frames only differ by an angle in the $xz$ plane. The CS and GJ framework refers to the rest frame of the pion pair, which can be reached by making use of two Lorentz transformations. It is important to note that for Run 1 of the ALICE experiment we worked under the Gottfried-Jackson reference frame.

Subsequent to the establishment of this frame of reference, the decay angles $\theta$ and $\phi$ for one of the pions of the system were established. The relevance of these angles is that they can be used for the calculation of the decay amplitude, which will be discussed later. The next step is to study the two-dimensional distributions of the pair of angles mentioned, which can be represented from an intensity function described in terms of the partial amplitudes and unnatural parity.

The intensity function can be expressed in terms of the spherical harmonics with which the decay amplitudes with quantum numbers L and M can be indicated.

$$I_0(M_X, \Omega) = \left|H_M^-(M_X)\right|^2 = \Sigma n_{LM} t_{LM}(M_X) ReY_L^M(\Omega)$$

where $M_X$ is the mass of the pseudoscalar pair , $\Omega$ is the solid angle, $t_{LM}$ is the momentum of the spherical harmonics and $n_{LM}$ is a normalization coefficient. They subsequently established that the state with maximum spin is 2, from which the S, P and D waves are obtained.

Having established the waves, they proceeded to implement partial wave analysis, which can be done through two mechanisms. The first one consists in making use of the moment of the spherical harmonics and the second one in employing $J_M^{epsilon}$. The first mechanism allows us to suppress the number of partial waves by cancelling some moments of the spherical harmonics, which can be used to represent the intensity function, these $t_{LM}$ function as parameters that allow us to adjust the minimization procedures in order to obtain a fixed value for each $t_{LM}$.

On the other hand, it is important to note that the intensity function can also be expressed in terms of the spin and parity amplitudes, likewise, these partial amplitudes can be used as fitting parameters, with the difference that in this case eight complex numbers would be obtained for each of the partial amplitudes which satisfy the $t_{LM}$ for the S, P and D waves.

The second mechanism is related to $J_M^{\epsilon}$, which, like the first mechanism, consists of suppressing the number of partial waves to obtain as a result, partial amplitudes given by the following expression:

$$H_M^- = S_0^- + D_0^- + D_1^-, H_M^+ = D_1^+$$

Consequently, they used minimization methods with which they obtained the first minimized points that were used as reference to make the continuity of the partial amplitudes, finally they calculated the Barrelet zeros from which the errors of these zeros were quantified and several graphs were obtained, where the signals corresponding

to the resonances $f_0(980)$ and $f_2(1270)$ can be seen, having these physical solutions, they proceeded to make a mass-dependent adjustment in order to know the mass and widths of the particles produced in the collision.

As a result of this last adjustment they proceeded to calculate the cross sections of the $f_0(980)$ and $f_2(1270)$ resonances with each of the partial waves. Finally they showed the mass, width and cross section with their respective systematic errors for both resonances, as well as, the differential cross section of the $\pi^+\pi^-$ system obtained from the partial wave analysis.

# Chapter 3

# Data Selection

The ALICE- LHC experiment collected diffractive events in proton-proton collisions at 13 TeV during 2017, where two and four pions were produced.

## 3.1 Run selection

To select the data sample we used the ALICE LogBook, where events triggered by CCUP13-B-SPD1-CENTNOTRD and CCUP25-B-SPD1-CENTNOTRD were selected, It is important to note that the B refers to having the beam from both sides, the SDP1 indicates that the SPD is used, in addition to assuring that the Bounch Crossings are analyzed, and finally, the CENTNOTRD assures that it is central and that the TRD is not used.

In addition to the two triggers, different beam parameters, detectors, among others, were selected in order to have an experimental sample that can be analyzed for the study of pion production in central diffractive processes. The selected criteria are listed below:

- Beam: Yes
- Beam Type: p-p
- Beam Mode Filter: Stable Beams

- Beam Energy (GeV): Min:6499
- Data Taking Quality Flag: Good Run
- Quality flag " not bad run" for AD, SPD, TOF, TPC and V0

Consequently, for 2017, 717 runs were selected and analyzed with the CCUP13-B-SPD1-CENTNOTRD trigger and 716 with the CCUP25-B-SPD1-CENTNOTRD trigger, which belong to the LHC17 f,h,i,k,l,m,o,r periods.

It is important to note that for the two and four pion study the same runs reported through the ALICE LogBook are used. The runs analyzed for 2017 are presented in the following table:

It is important to note that there are runs that despite complying with the considerations made in ALICE's LogBook could not be downloaded, these runs are shown below

## 3.2 Event Selection

From the selected sample described in previous session, we consider those events with exactly 2 or 4 good reconstructed quality tracks in the TPC. To optimize the event selection we applied the cuts described below:

- Particle Identification criteria (PID) is equal to $\sigma^2_{\pi_1} + \sigma^2_{\pi_2} < 4$
- $P_t < 0.5$ (In the case of two pions) / $P_t < 1.0$ (In the case of four pions)
- !V0
- !AD
- $\mid Vtx \mid < 10$

| Period | Run Numbers |
|---|---|
| LHC17r | 282704,282703,282702,282700,282677,282676,282673,282671,282670, 282667,282666,282651,282629,282622,282620,282618,282609,282608, 282607,282606,282580,282579,282575,282573,282546,282545,282544, 282528 |
| LHC17o | 281961,281956,281953,281940,281939,281932,281931,281928,281920, 281918,281916,281915,281895,281894,281893,281756,281755,281754, 281753,281751,281750,281741,281713,281709,281706,281705,281633, 281592,281583,281581,281580,281574,281569,281568,281563,281562, 281557,281511,281509,281477,281475,281450,281449,281446,281444, 281443,281441,281415,281350,281321,281301,281277,281275,281273, 281271,281244,281243,281242,281241,281240,281213,281212,281191, 281190,281189,281181,281180,281179,281081,281080,281079,281062, 281061,281060,281036,281035,281033,281032,280999,280998,280997, 280996,280994,280990,280947,280943,280940,280936,280897,280880, 280856,280854,280849,280848,280847,280844,280842,280793,280792, 280787,280786,280768,280767,280766,280765,280764,280763,280762, 280761,280757,280756,280755,280754,280753,280729,280706,280705, 280681,280679,280676,280673,280671,280650,280648,280647,280645, 280639,280637,280636,280634,280613,280583,280581,280575,280574, 280551,280550,280547,280546,280519,280518,280499,280490,280448 |
| LHC17o | 280447,280446,280445,280443,280419,280415,280412,280406,280405, 280403,280375,280374,280352,280351,280350,280349,280348,280312, 280310,280290,280286,280285,280284,280282 |
| LHC17m | 280140,280135,280134,280131,280126,280118,280114,280111,280108, 280107,280066,280052,280051,279855,279854,279853,279830,279827, 279826,279773,279749,279747,279719,279718,279715,279689,279688, 279687,279684,279683,279682,279679,279677,279676,279642,279641, 279632,279630,279559,279550,279491,279488,279487,279483,279441, 279439,279435,279410,279391,279355,279354,279349,279348,279344, 279342,279312,279310,279309,279274,279273,279270,279268,279267, 279265,279264,279242,279238,279235,279234,279232,279208,279207, 279201,279199,279157,279155,279130,279123,279122,279118,279117, 279107,279106,279075,279074,279073,279069,279068,279044,279043 |

| | |
|---|---|
| LHC17m | 279041,279036,279035,279008,279007,279005,279000,278999,278964, 278963,278960,278959 |
| LHC17l | 278216,278215,278191,278189,278167,278166,278165,278164,278163, 278158,278130,278127,278126,278123,278122,278121,277996,277991, 277989,277988,277987,277952,277930,277907,277904,277903,277900, 277899,277898,277897,277876,277870,277848,277847,277845,277842, 277841,277836,277834,277805,277802,277801,277800,277799,277795, 277794,277749,277747,277746,277745,277725,277723,277722,277721, 277577,277576,277575,277574,277537,277536,277534,277531,277530, 277479,277478,277477,277476,277473,277472,277470,277418,277417, 277416,277389,277386,277385,277384,277383,277360,277314,277312, 277310,277293,277262,277257,277256,277197,277196,277194,277193, 277189,277188,277184,277183,277182,277181,277180,277155,277121, 277117,277091,277087,277082,277079,277076,277073,277037,277017, 277016,277015,276972,276971,276970,276969,276967,276920,276917, 276916,276762,276675,276674,276672,276671,276670,276669,276644, 276608,276557,276556,276553,276552,276551 |
| LHC17k | 276508,276507,276506,276462,276439,276438,276435,276429,276351, 276348,276302,276297,276294,276292,276290,276259,276257,276230, 276205,276178,276177,276170,276169,276166,276145,276141,276140, 276135,276108,276105,276104,276102,276099,276098,276097,276045, 276041,276040,275925,275924,275664,275661,275650,275648,275647, 275624,275623,275622,275621,275617,275614,275612,275559,275558, 275515,275472,275471,275467,275459,275457,275456,275453,275452, 275448,275443,275406,275404,275401,275395,275394,275372,275369, 275361,275360,275333,275332,275328,275326,275324,275322,275314, 275283,275247,275246,275245,275239,275150,275149,275076,275075, 275073,275068,274978,274889,274886,274884,274883,274882,274878, 274877,274822,274821,274815,274807,274806,274803,274802,274801, 274736 |
| LHC17i | 274442,274364,274363,274360,274357,274355,274352,274329,274283, 274281,274280,274279,274278,274276,274271,274270,274269,274268, 274266,274264,274263,274259,274258,274232,274212,274174,274148, 274147,274125,274094,274092,274063,274058,273986,273985,273946, 273943,273942,273918,273889,273887,273885,273825 |
| LHC17h | 273103,273101,273100,273099,273077,273010,273009,272985,272983, 272976,272949,272947,272939,272935,272934,272933,272932,272905, 272903,272880,272873,272871,272870,272836,272835,272834,272833, 272829,272828,272784,272783,272782,272764,272763,272762,272760, 272749,272747,272746,272712,272691,272690,272620,272610,272608, 272607,272585,272577,272575,272574,272521,272469,272468,272466, 272463,272462,272461,272417,272414,272413,272411,272400,272399, 272395,272394,272389,272388,272360,272359,272340,272335,272194, 272156,272155,272154,272153,272152,272151 |
| LHC17f | 270865 |

Table 3.1: List of runs analyzed for the year 2017.

| Period | Run Numbers |
|---|---|
| LHC17r | 282615 |
| LHC17o | 281946, 281919, 281634,281188,281187,281186,280418 |
| LHC17m | 279893,279889,279886,279884,279879,279561,279560,279125,279038, 279037,278994 |
| LHC17l | 278162,278095,278094,278093,278092,278091,278089,278082,278080, 278079,278077,278055,277748,277720,277718,277250,277088,277075, 276643 |
| LHC17k | 276500,276461,276434,276432,276107,275613,275473,275357,275070, 274945,274943,274901,274895,274892,274873 |
| LHC17i | 274057 |
| LHC17h | 272619 |

Table 3.2: Runs that could not be downloaded for the year 2017.

- $VtxChi2 < 100$

The first consideration applied to the experimental sample corresponds to the PID, from which it is possible to determine the probability that a particle belongs to a certain species, in our case the PID indicates all possible pion pairs that are less than 2 $\sigma$. The second consideration used corresponds to the transverse momentum in which values lower than 0.5 GeV/c (or 1 GeV/c) are requested, because in this range the highest concentration of data is found.

The third and fourth considerations correspond to the vetoes in the V0 and AD detectors respectively, which consist of not registering particle production when having a valid event in these detectors. The penultimate consideration is related to the primary vertex and applies to those particles whose vertex has been reconstructed between 10 cm and -10 cm from the interaction point, finally, the VtxChi2 consideration refers to a quality cut in the selection of the track.

# Chapter 4

# Analysis and results

In this section we present the analysis of two and four pion events. The analysis was done with the official offline framework of ALICE, AliRoot, and Root version 5.34/30.

## 4.1 Analysis for $\pi^+\pi^-$

The reconstructed histograms from the experimental sample were made by implementing a quadrivector, which is composed of the transverse momentum, the pseudorapidity, the azimuthal angle and the assumption that the particle has the pion mass of $139.57061 \pm 0.00023$ MeV.

It is important to note that from this quadrivector the "Mother" particle can be reconstructed as the sum of two quadrivectors corresponding to the "Daughter" particle $\pi^+$ and $\pi^-$ respectively.

In the two-pion analysis, a total of $7.315326x10^7$ events were recorded, to which each of the above-mentioned considerations were gradually applied; the number of events with respect to each applied cut is presented below.

| **Cuts** | **Number of events** |
|---|---|
| Invariant Mass (IM) | 7.315326e+07 |
| IM+PID | 5.082673e+07 |
| IM + PID + $P_t$ | 2.091868e+07 |
| IM + PID + $P_t$ +!V0 | 1.124767e+07 |
| IM + PID + $P_t$ + !V0 + !AD | 5250208 |
| IM + PID + $P_t$ + !V0 + !AD + Vtx | 5163675 |
| IM + PID + $P_t$+ !V0 + !AD + Vtx + VtxChi2 | 5056231 |

Table 4.1: Cuts applied to the experimental data sample for 2 pion events in central diffractive processes.

One of the most significant histograms of this analysis is the one related to the invariant mass distribution of $\pi^+\pi^-$ system. The evolution of the invariant mass distribution for $\pi^+\pi^-$ events is shown below for each of the applied cuts.

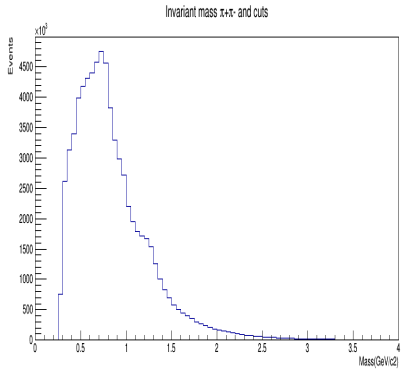


Figure 4.1: Invariant mass of $\pi^+\pi^-$ system.

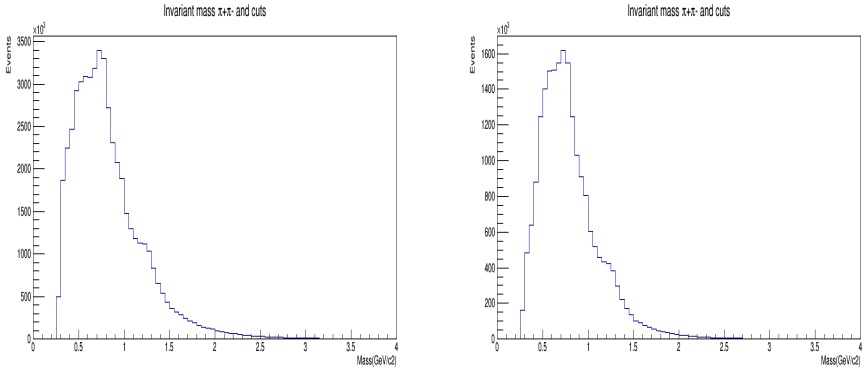


Figure 4.2: Invariant mass of $\pi^+\pi^-$ system, after PID selection (left) and PID selection with a Pt cut (right).

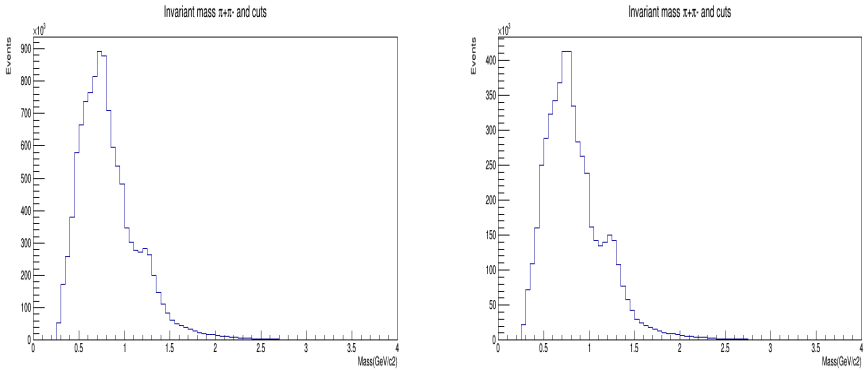


Figure 4.3: Invariant mass of $\pi^+\pi^-$ system, after PID selection with Pt cut and V0 veto (left) and PID selection with a Pt cut and V0 and AD veto (right).

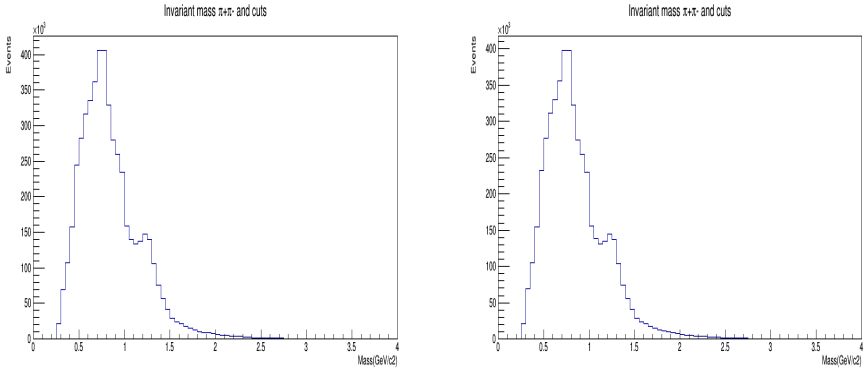


Figure 4.4: Invariant mass of $\pi^+\pi^-$ system, after PID selection with Pt cut, V0 and AD veto with primary vertex selection (left) and PID selection with Pt cut, V0 and AD veto with primary vertex selection and quality track cut (right).

In each histogram, it is possible to observe a notorious reduction of events for the different applied cuts, likewise, it is possible to observe the presence of some resonances, such as: $K_s^0(500)$, $\rho^0(770)$ , $f_0(980)$ and $f_2(1270)$ .

On the other hand, the plots corresponding to the PID with the aforementioned cuts are presented. It is important to point out that the PID, besides making reference to the particle species, presents the opportunity to know the mass and the constitution of them, this consideration acts in the experimental sample as a restriction to prevent the contamination of particles belonging to other species.

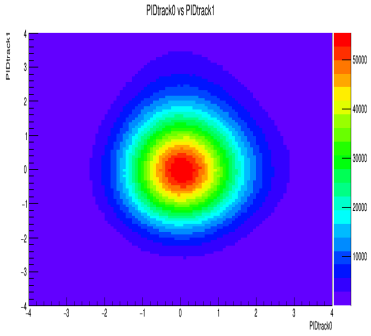


Figure 4.5: Reconstructed PID for $\pi^+\pi^-$. No cuts applied here.

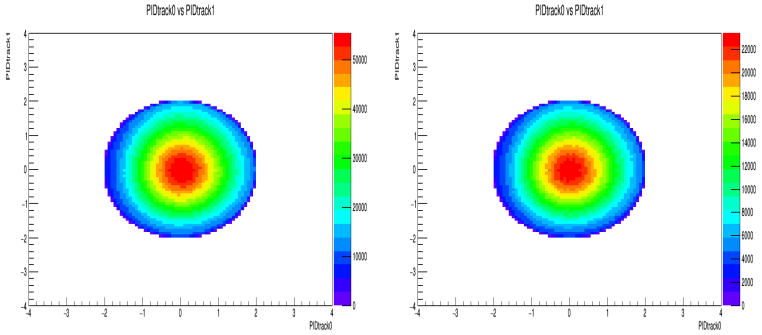


Figure 4.6: PID of $\pi^+\pi^-$ system, after PID selection (left) and PID selection with a Pt cut (right).

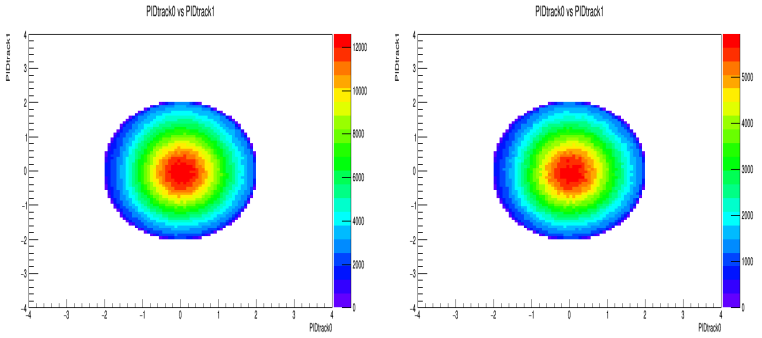


Figure 4.7: PID of $\pi^+\pi^-$ system, after PID selection with Pt cut and V0 veto (left) and PID selection with a Pt cut and V0 and AD veto (right).

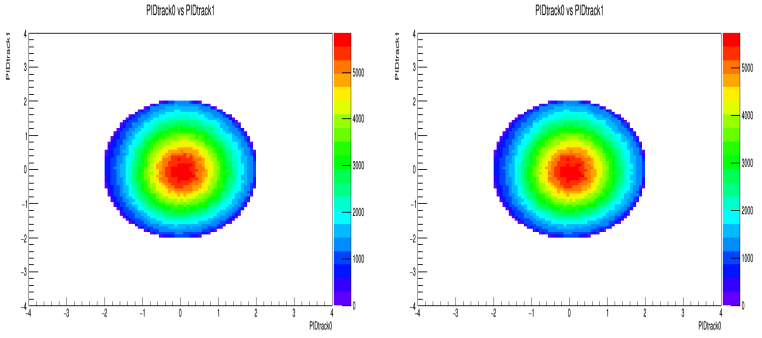


Figure 4.8: PID of $\pi^+\pi^-$ system, after PID selection with Pt cut, V0 and AD veto with primary vertex selection (left) and PID selection with Pt cut, V0 and AD veto with primary vertex selection and quality track cut (right).

In the previous plots, as well as in the mass spectra, it is possible to notice the decrease of entries, as each of the considerations were made, in the same way, this decrease of events can be noticed in the next plots of invariant mass versus transverse momentum.

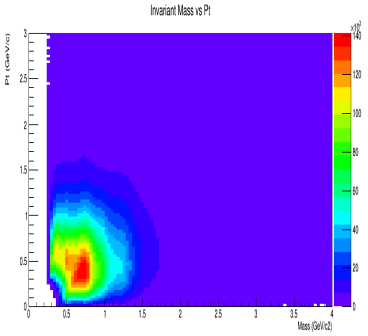


Figure 4.9: Reconstructed invariant mass versus transverse momentum of $\pi^+\pi^-$. No cuts applied here.

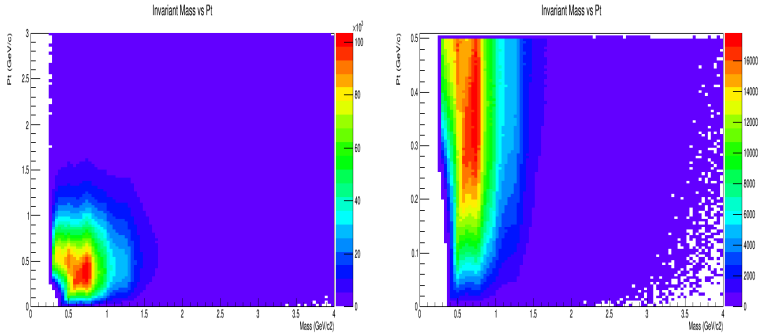


Figure 4.10: Invariant mass versus transverse momentum of $\pi^+\pi^-$ system, after PID selection (left) and PID selection with a Pt cut (right).

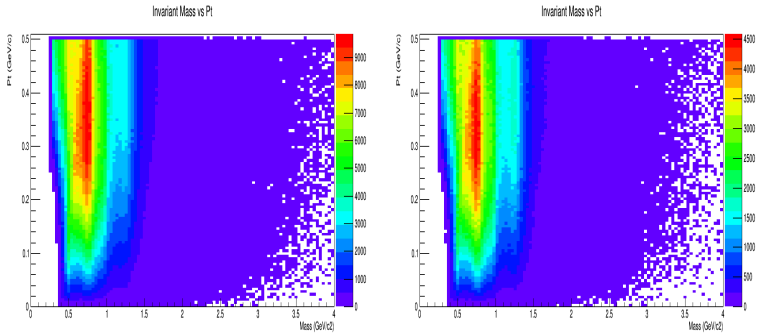


Figure 4.11: Invariant mass versus transverse momentum of $\pi^+\pi^-$ system, after PID selection with Pt cut and V0 veto (left) and PID selection with a Pt cut and V0 and AD veto (right).

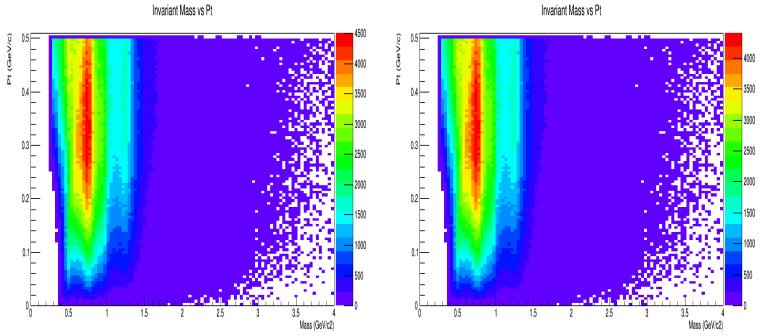


Figure 4.12: Invariant mass versus transverse momentum of $\pi^+\pi^-$ system, after PID selection with Pt cut, V0 and AD veto with primary vertex selection (left) and PID selection with Pt cut, V0 and AD veto with primary vertex selection and quality track cut (right).

Subsequently, the plots of the V0 and AD offline decisions are shown, where each of the four decisions has a different meaning:

- 0 $\longrightarrow$ The detector is empty.
- 1 $\longrightarrow$ Detector has signal in the beam window .
- 2 $\longrightarrow$ Detector has signal at the beam-gas window.
- 3 $\longrightarrow$ The signal reached the detector at a time different from the time windows (beam and gas).

Based on these decisions, the plots corresponding to the offline decisions are shown below

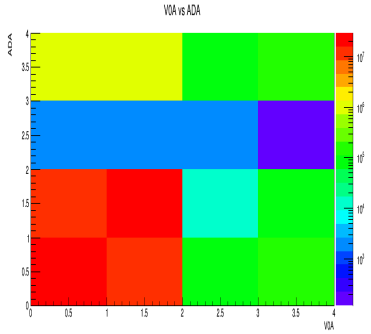


Figure 4.13: V0A versus ADA of $\pi^+\pi^-$ system.No cuts applied here.

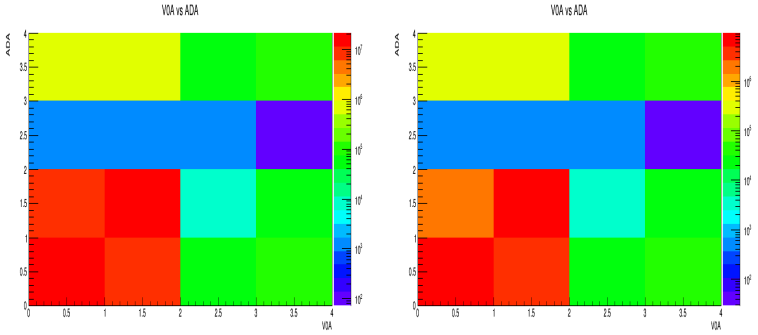


Figure 4.14: V0A versus ADA of $\pi^+\pi^-$ system, after PID selection (left) and PID selection with a Pt cut (right).

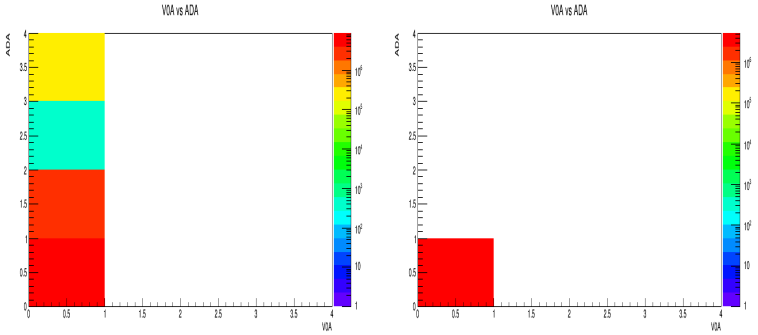


Figure 4.15: V0A versus ADA of $\pi^+\pi^-$ system, after PID selection with Pt cut and V0 veto (left) and PID selection with a Pt cut and V0 and AD veto (right).

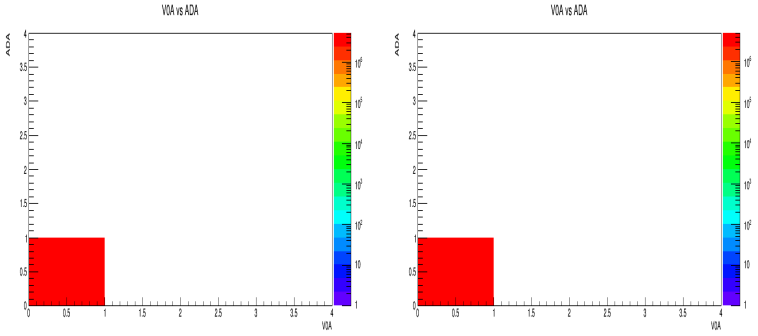


Figure 4.16: V0A versus ADA of $\pi^+\pi^-$ system, after PID selection with Pt cut, V0 and AD veto with primary vertex selection (left) and PID selection with Pt cut, V0 and AD veto with primary vertex selection and quality track cut (right).

## 4.2 Angular Analysis for $\pi^+\pi^-$

An angular analysis can be visualized from different reference frames such as Collins-Soper, Gottfried-Jackson or Helicity . The purpose of this section is to study the angular distribution $\pi^+$ within the Collins-Soper (CS) reference frame.

The angular distributions of $(\phi_\pi, \cos\theta_\pi)$ presented below were made with the same considerations that were applied to the plots of the previous section.

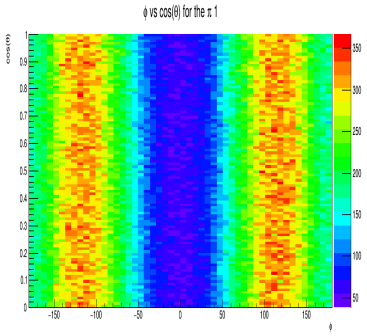


Figure 4.17: Angular distributions of $\pi^+\pi^-$ system.No cuts applied here.

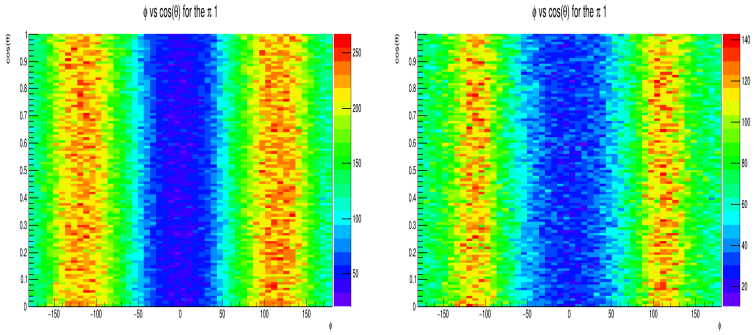


Figure 4.18: Angular distributions of $\pi^+\pi^-$ system, after PID selection (left) and PID selection with a Pt cut (right).

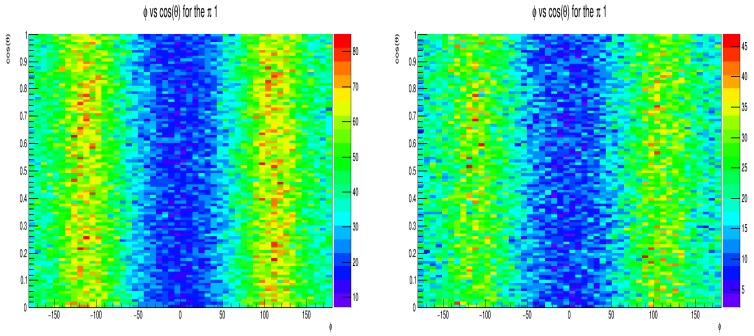


Figure 4.19: Angular distributions of $\pi^+\pi^-$ system, after PID selection with Pt cut and V0 veto (left) and PID selection with a Pt cut and V0 and AD veto (right).

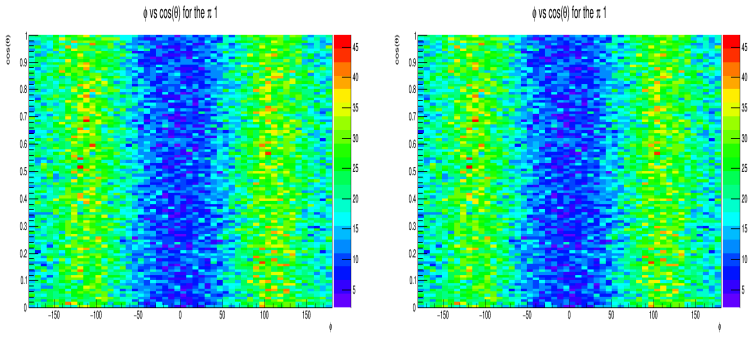


Figure 4.20: Angular distributions of $\pi^+\pi^-$ system, after PID selection with Pt cut, V0 and AD veto with primary vertex selection (left) and PID selection with Pt cut, V0 and AD veto with primary vertex selection and quality track cut (right).

As can be noted, the two-dimensional distributions between $\phi$ and $\cos\theta$ do not present significant changes when performing each of the considerations. On the other hand, further restrictions were made to the experimental sample in the mass and in $\eta$, for this purpose we present such restrictions in two cases: the first case, consists of adding a consideration just after the PID, this cut is based on establishing a region for the invariant mass within the range of $0.6 - 1.0 GeV/c^2$), based on this the following plots are shown.

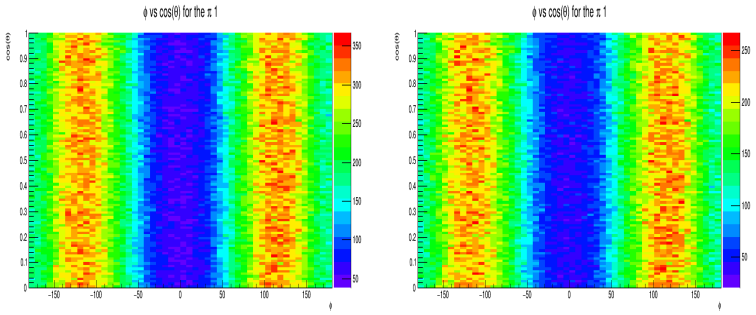


Figure 4.21: Angular distributions of $\pi^+\pi^-$ system.No cuts applied here (left) and PID selection (right).

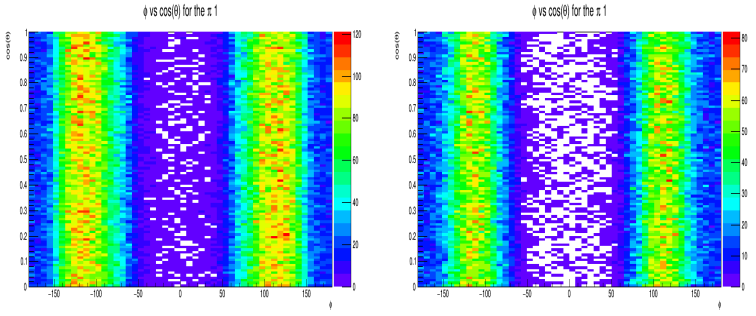


Figure 4.22: Angular distributions of $\pi^+\pi^-$ system, PID selection with a Mass cut (left) and PID selection with Mass and Pt cuts (right).

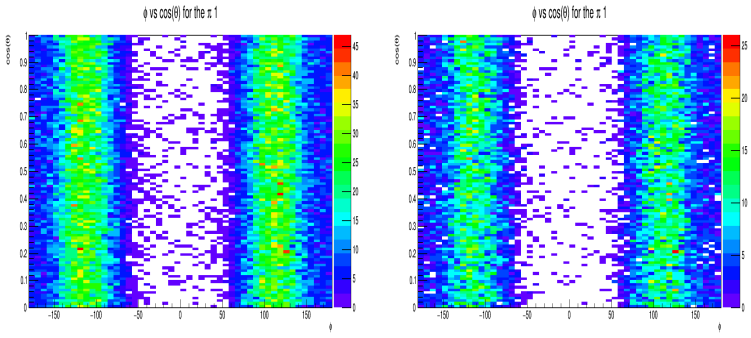


Figure 4.23: Angular distributions of $\pi^+\pi^-$ system, after PID selection with Mass and Pt cuts and V0 veto (left) and PID selection with a Mass and Pt cuts and V0 and AD veto (right).

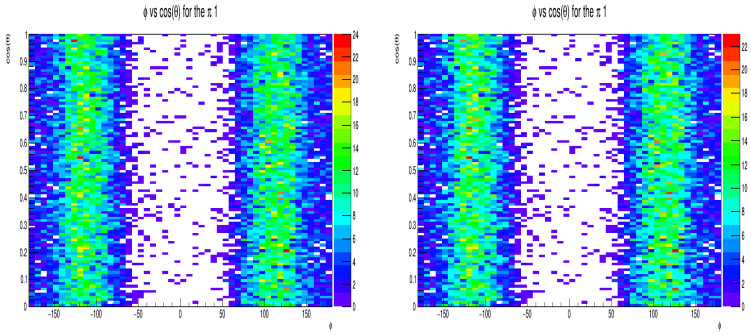


Figure 4.24: Angular distributions of $\pi^+\pi^-$ system, after PID selection with Mass and Pt cuts, V0 and AD veto with primary vertex selection (left) and PID selection with Mass and Pt cuts, V0 and AD veto with primary vertex selection and quality track cut (right).

Note that unlike the plots with the standard considerations, applying the cuts in the mass causes a change in the two-dimensional distributions, the appearing structures change immediately and exhibits the same behaviour for all the cuts.

Subsequently, the second case is presented, which consists of adding three more considerations to those presented initially, these cuts consist of incorporating an invariant mass region within the range of $1.0-1.5 GeV/c^2$, establishing the transverse momentum of a pion, which must be greater than 0.15 GeV ( $P_{t,\pi} > 0.15$ GeV) and $\mid \eta_\pi \mid < 0.7$. Implementing all considerations we obtain the following two-dimensional distributions in $(\phi_\pi, \cos\theta_\pi)$

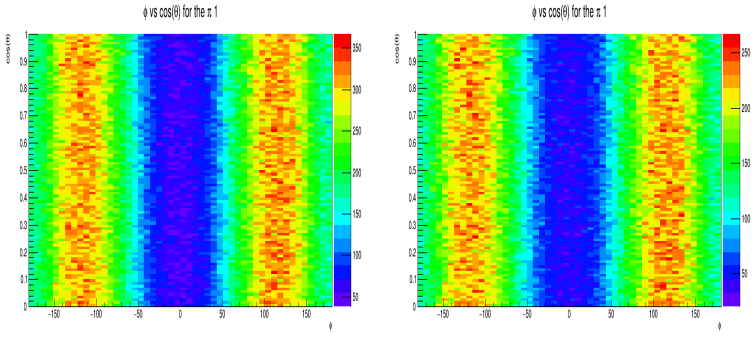


Figure 4.25: Angular distributions of $\pi^+\pi^-$ system.No cuts applied here (left) and PID selection (right).

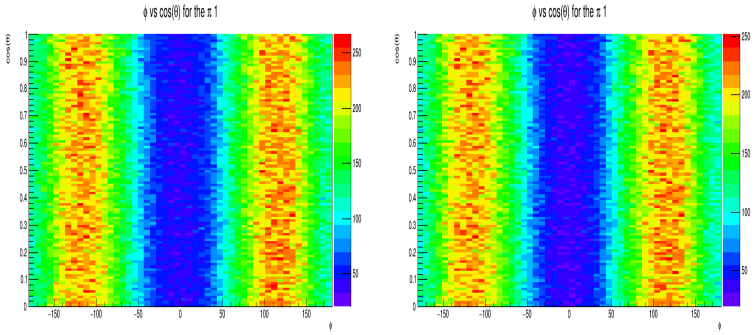


Figure 4.26: Angular distributions of $\pi^+\pi^-$ system, PID selection with a Mass cut (left) and PID selection with Mass and Pt cuts (right).

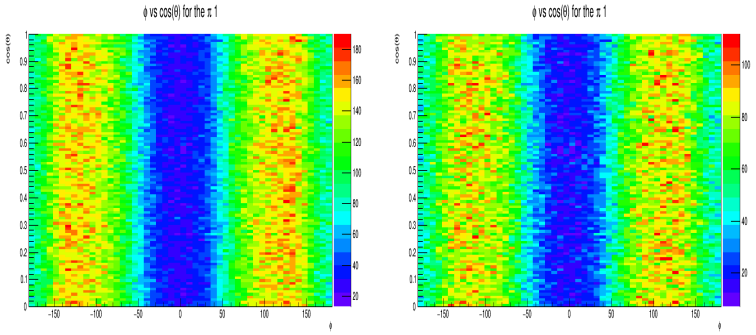


Figure 4.27: Angular distributions of $\pi^+\pi^-$ system, after PID selection with Mass and Pt and $\eta$ cuts (left) and PID selection with a Mass and Pt and $\eta$ cuts and V0 veto (right).

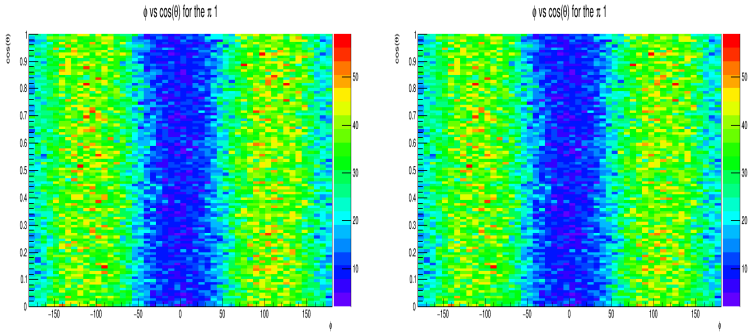


Figure 4.28: Angular distributions of $\pi^+\pi^-$ system, after PID selection with Mass and Pt and $\eta$ cuts, V0 and AD veto (left) and PID selection with Mass and Pt and $\eta$ cuts, V0 and AD veto with primary vertex selection and quality track cut (right).

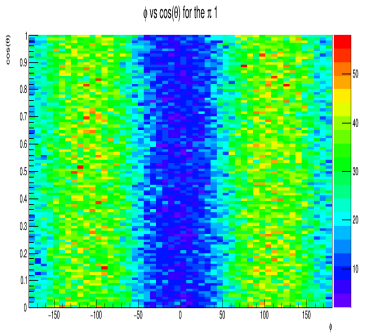


Figure 4.29: Angular distributions of $\pi^+\pi^-$ system, after PID selection with Mass and Pt and $\eta$ cuts, V0 and AD veto with primary vertex selection and quality track cut (right).

It is possible to note that the structures presented in the previous graphs do not show significant changes as the cuts are applied.

## 4.3 Monte Carlo for $\pi^+\pi^-$

For Monte Carlo analysis we used the /alice/sim/2016/LHC16c1b, c, d, e files which were generated in DRgen for Run 1 of the ALICE experiment. The DRgen generator aims to simulate a $\pi^+\pi^-$ decaying X-system from the double pomeron exchange.

In this section the angular plots in the CS frame obtained from DRgen are presented, it should be noted that not all standard considerations were implemented since for Run 1 the AD detector was not installed in ALICE. The following two-dimensional distributions for polar and azimuthal angles correspond to the standard considerations, which were applied to the data collected for 2017.

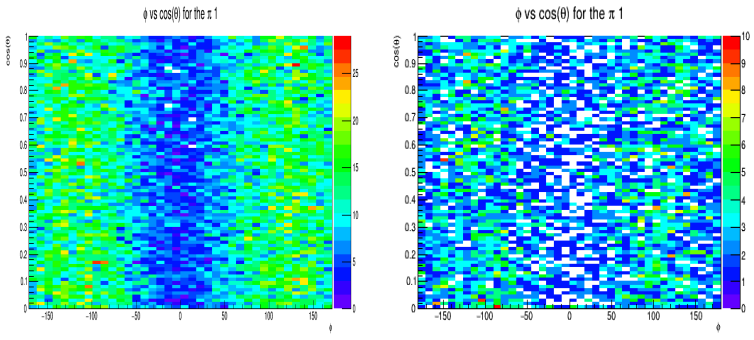


Figure 4.30: Angular distributions of $\pi^+\pi^-$ system.No cuts applied here (left) and PID selection (right).

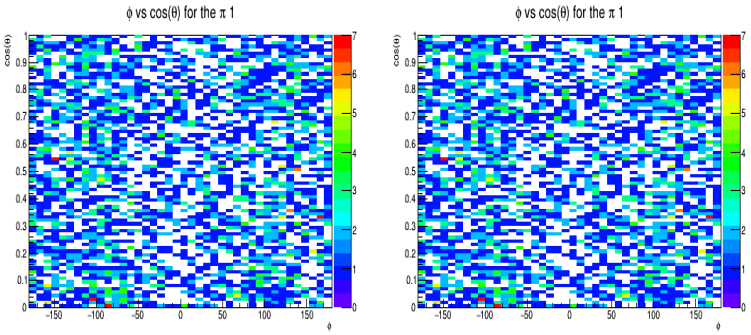


Figure 4.31: Angular distributions of $\pi^+\pi^-$ system, after PID selection with a Pt cut(left) and PID selection with a Pt cut and V0 veto (right).

Similarly, angular plots were obtained from applying a cut in the mass $0.6-1.0GeV/c^2$ with the DRgen.

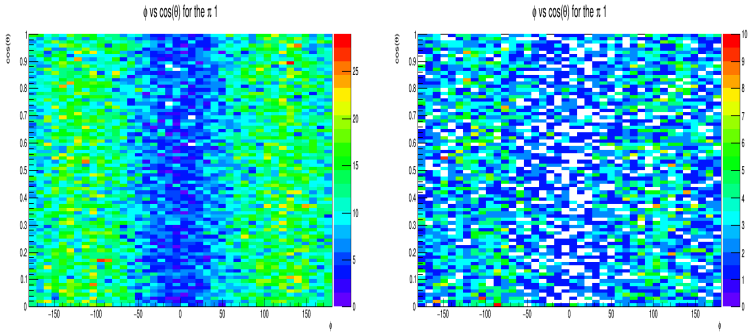


Figure 4.32: Angular distributions of $\pi^+\pi^-$ system.No cuts applied here (left) and PID selection (right).

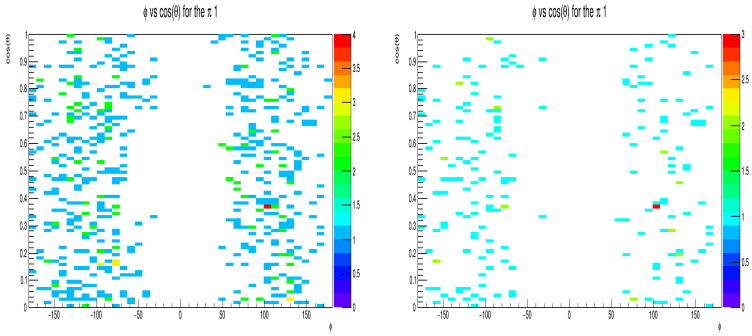


Figure 4.33: Angular distributions of $\pi^+\pi^-$ system, PID selection with a Mass cut (left) and PID selection with Mass and Pt cuts (right).

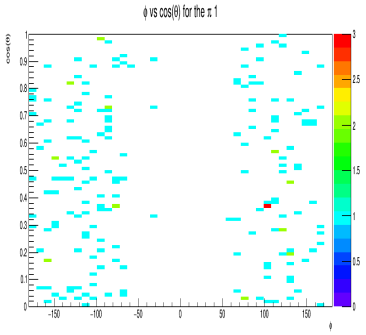


Figure 4.34: Angular distributions of $\pi^+\pi^-$ system, after PID selection with Mass and Pt cuts and V0 veto.

Finally, two-dimensional distributions of $(\phi_\pi, \cos\theta_\pi)$ are presented considering those events with an invariant mass of the $\pi^+ - \pi^-$ system between $1.0 - 1.5 GeV/c^2$, a $P_t > 0.15 GeV$ and $\mid \eta \mid < 0.7$ .

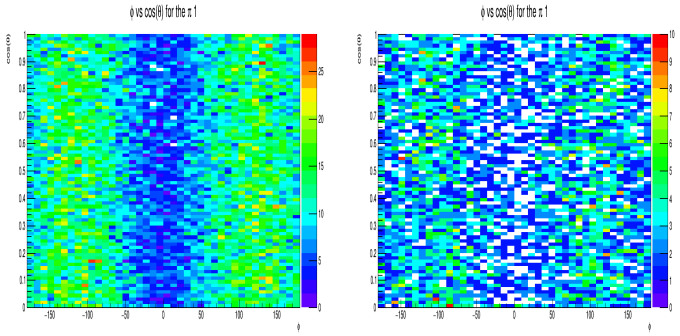


Figure 4.35: Angular distributions of $\pi^+\pi^-$ system.No cuts applied here (left) and PID selection (right).

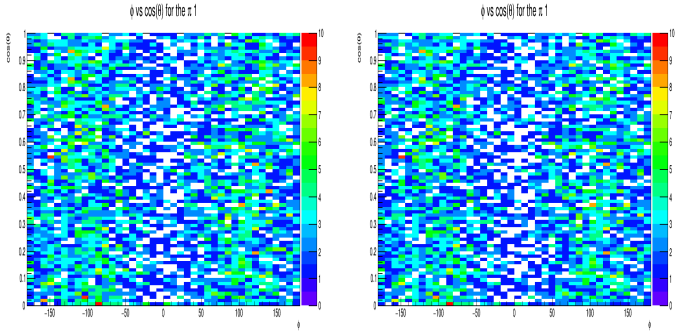


Figure 4.36: Angular distributions of $\pi^+\pi^-$ system, PID selection with a Mass cut (left) and PID selection with Mass and Pt cuts (right).

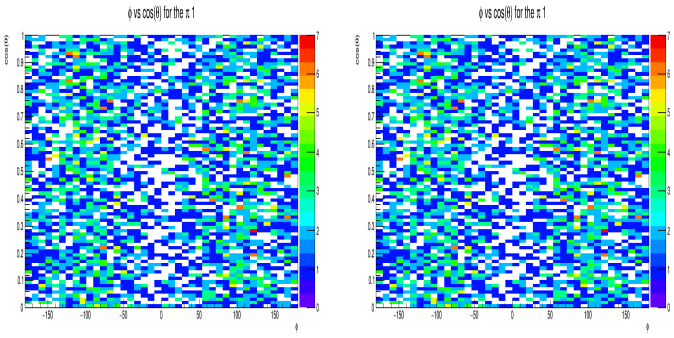

Figure 4.37: Angular distributions of $\pi^+\pi^-$ system, after PID selection with Mass and Pt and $\eta$ cuts (left) and PID selection with a Mass and Pt and $\eta$ cuts and V0 veto (right).

## 4.4 Results for $\pi^+\pi^-$

Our invariant mass distribution is qualitatively compared with the one from COMPASS experiment [7] and the previously obtained by ALICE for proton+proton collisions at 7 TeV. The comparison is shown in Fig. 4.38

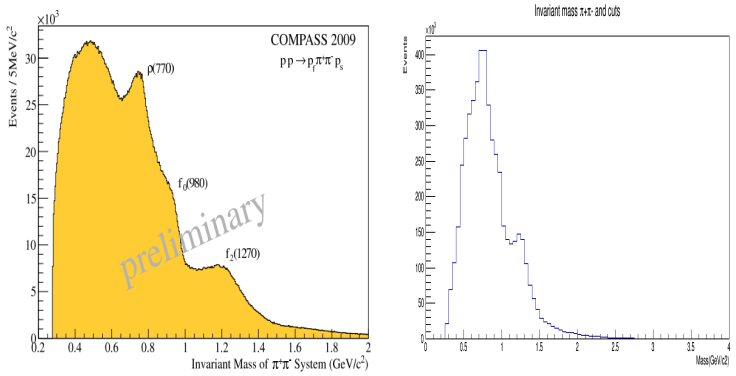


Figure 4.38: The image on the left corresponds to the plot obtained from the COMPASS experiment [7] and the one on the right is the invariant mass with PID selection with Pt cut, V0 and AD veto with primary vertex selection.

From Fig. 4.38, it is possible to identify the presence of the resonances $\rho^0(770)$ , $f_0(980)$ and $f_2(1270)$, which are some glueball candidates. In Fig. 4.39 we present a qualitatively comparison between our results and those from Run 1 for proton-proton collisions at 7 TeV. The same resonances are identified in both, such as $K^0_s(500)$, $\rho^0(770)$, $f_0(980)$ and $f_2(1270)$ within which we again find two glueball candidates, such as $f_0(980)$ and $f_2(1270)$.

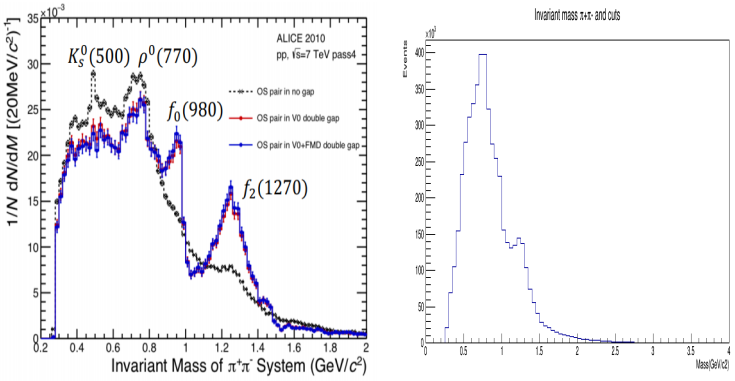


Figure 4.39: The image on the left corresponds to the plot obtained in Run 1 of the ALICE experiment [15] and the one on the right is the invariant mass with PID selection with Pt cut, V0 and AD veto with primary vertex selection and quality track cut (right).

### 4.4.1 Angular results for $\pi^+\pi^-$

On the other hand, we have the analysis of the two-dimensional distributions of the azimuthal and polar angles, based on which we can compare some of the plots reconstructed from the data collected with those reported in the paper **Extracting the Pomeron-Pomeron-$f_2(1270)$ coupling in the $pp \longrightarrow pp\pi^+\pi^-$ reaction through the angular distribution of the pions** by Lebiedowicks P. et al.

In this paper we show the two-dimensional distributions between the azimuthal and polar angles, in which various structures are observed to be produced, starting from the reaction $pp \longrightarrow pp\pi^+\pi^-$. In addition, the different couplings are shown for $ppf_2(1270)$ , as well as for the production of the continuum. It is important to note that the couplings shown throughout this article generate different patterns, which must be verified experimentally.

The first angular plot that we will compare with the previously described paper, is the one reconstructed with the PID + Pt cut and the one generated with DRGen without any consideration, where it can be observed that the plots present a very similar structure between them.

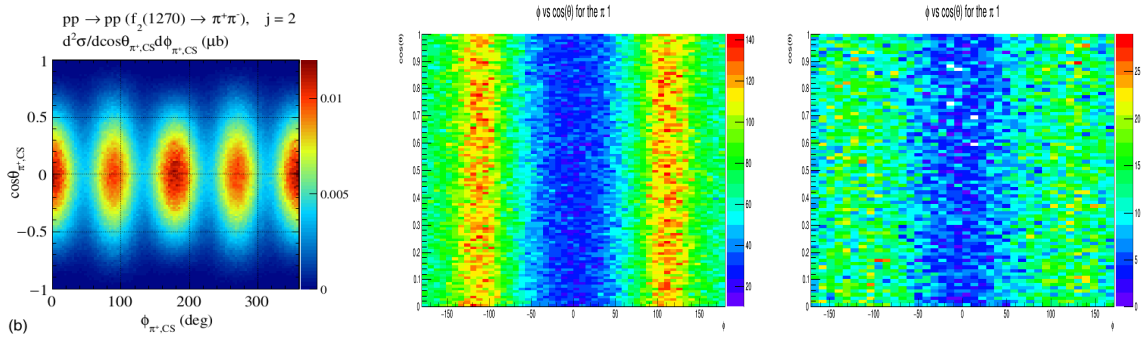


Figure 4.40: The image on the left is the one presented in the article by Lebiedowicks P. et al, the one in the center corresponds to data sample (this thesis) and the image on the right from Monte Carlo by DRgen.

The second plot to be compared is related to the one obtained after the PID cut, where the invariant mass is within the range of $0.6 - 1.0 GeV/c^2$, and the Monte Carlo sample was treated as the experimental data. In these three plots, the mean value seems to be of the same order.

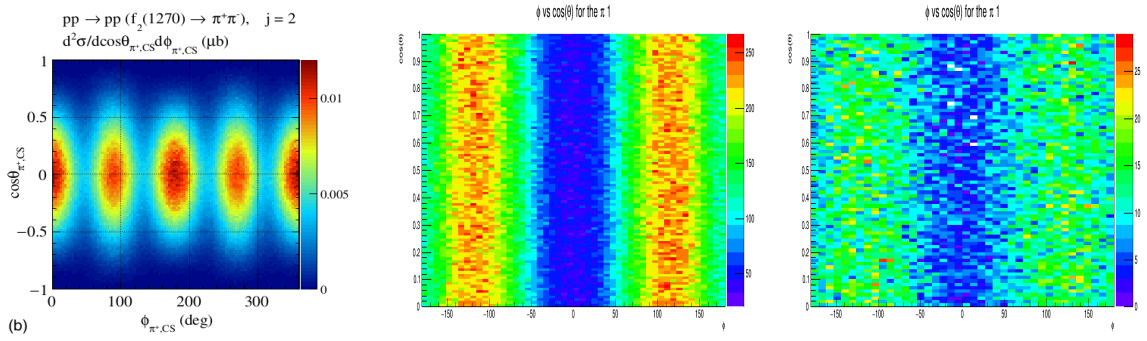


Figure 4.41: The image on the left is the one presented in the article by Lebiedowicks P. et al, the one in the center corresponds to the one reconstructed from the experimental data (this thesis) and the image on the right is the one generated with DRgen.

Finally, we compare the plots corresponding to the PID + Mass cut applied to the data, the one generated with DRgen without cuts and the one set out in Figure 7 of the paper by Lebiedowicks P. et al.

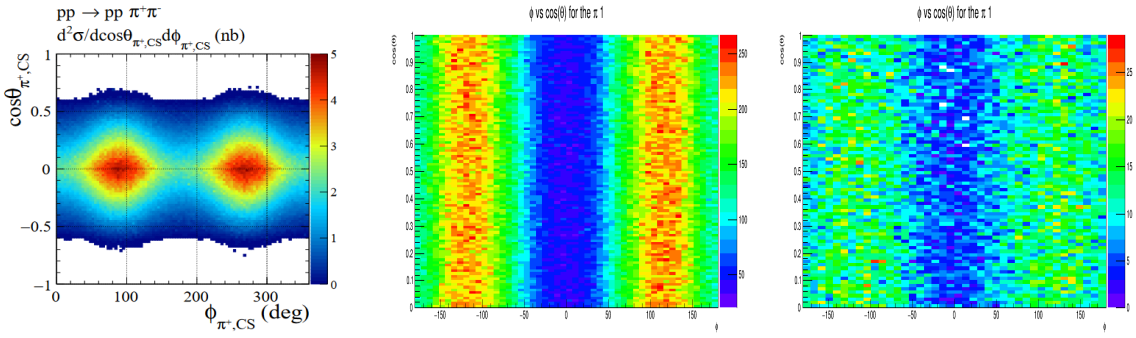


Figure 4.42: The image on the left is the one presented in the article by Lebiedowicks P. et al, the one in the center corresponds to the one reconstructed from the experimental sample (this thesis) and the image on the right is the one generated by DRgen.

It is important to note that the theoretical plot that most similar to the one reconstructed from the data corresponds to the one presented for the pions continuum and the one for the $ppf_2(1270)$ coupling given by j=2. These comparisons allow us to observe that to a large extent the shape of the distributions depends on the cuts made, as well as on the range of the cuts.

## 4.5 Analysis for $\pi^+\pi^-\pi^+\pi^-$

In the analysis of four pions, a total of $3.260922 \times 10^7$ events were recorded. In the same way as in the case of two pions, each of the cuts to the experimental sample were applied in order to reduce the noise generated by other processes, it should be noted that the same considerations used for two bodies were applied to this study, the only difference lies in the range established for the cut of the transverse momentum, in the case of four bodies it is established from 0-1 GeV/c. The following table shows the number of entries per applied cut.

The change in the invariant mass spectrum for four pions with all considerations applied to the experimental sample can be clearly seen in the following figures. Note that the decrease in inputs in this case causes the change in the spectrum to be stepwise.

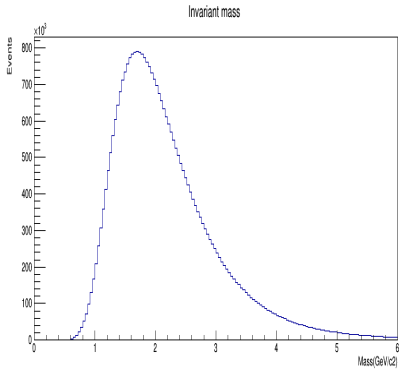


Figure 4.43: Invariant mass of $\pi^+\pi^-\pi^+\pi^-$ system.

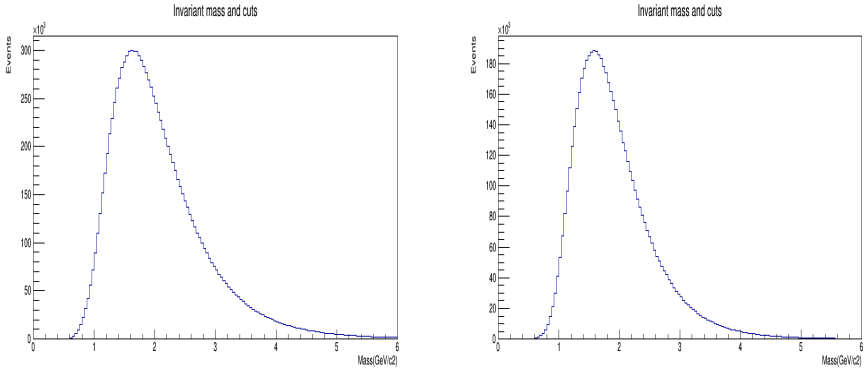


Figure 4.44: Invariant mass of $\pi^+\pi^-\pi^+\pi^-$ system, after PID selection (left) and PID selection with a Pt cut (right).

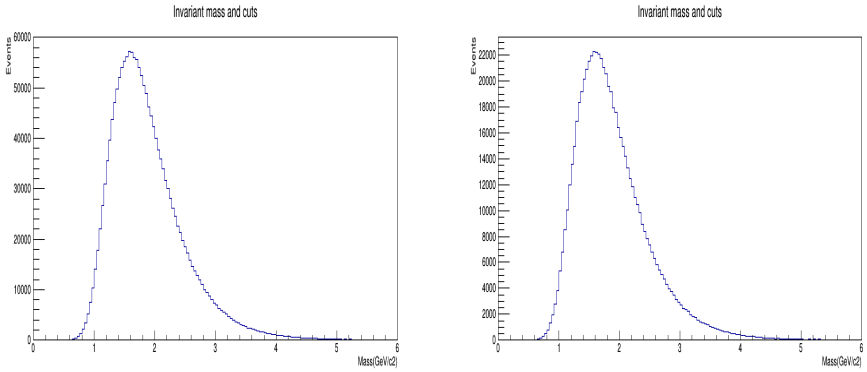


Figure 4.45: Invariant mass of $\pi^+\pi^-\pi^+\pi^-$ system, after PID selection with Pt cut and V0 veto (left) and PID selection with a Pt cut and V0 and AD veto (right).

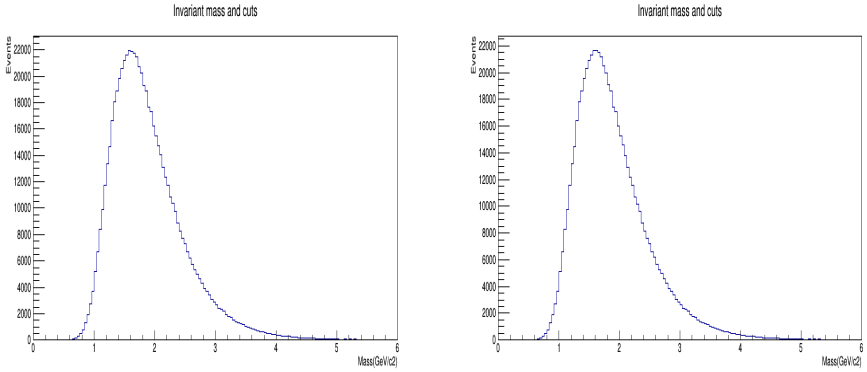


Figure 4.46: Invariant mass of $\pi^+\pi^-\pi^+\pi^-$ system, after PID selection with Pt cut, V0 and AD veto with primary vertex selection (left) and PID selection with Pt cut, V0 and AD veto with primary vertex selection and quality track cut (right).

| Cuts | Number of events |
|---|---|
| Invariant Mass (IM) | 3.260922e+07 |
| IM+PID | 1.142995e+07 |
| IM + PID + $P_t$ | 6117871 |
| IM + PID + $P_t$ +!V0 | 1744647 |
| IM + PID + $P_t$ + !V0 + !AD | 680555 |
| IM + PID + $P_t$ + !V0 + !AD + Vtx | 671226 |
| IM + PID + $P_t$+ !V0 + !AD + Vtx + VtxChi2 | 8814 |

Table 4.2: Cuts applied to the experimental data sample to select 4 pions events in central diffractive processes.

Similarly, we present the histogram corresponding to the mass of the lighter pair and the recoiling, this type of graph is made with the purpose of visualizing the contributions of both subsystems.

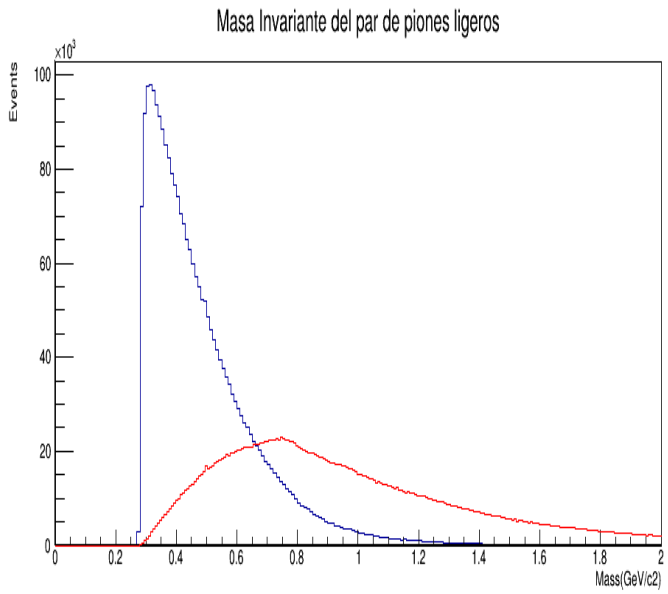


Figure 4.47: This figure shows the mass of the lightest pion pair (blue line) and the reoiling (red line).

## 4.6 Angular Analysis for $\pi^+\pi^-\pi^+\pi^-$

In the same way as for two bodies, the two-dimensional distribution analysis was made in $(\phi, \cos\theta)$ for the experimental sample of four bodies, in this case the study is focused on the pair of lighter pions and the recoiling. It is important to point out that for this case the cuts presented previously were applied, furthermore, it should be noted that

from the reconstruction of these two plots it was possible to rehearsal a study of angular distributions for the 4 pion sample.

We applied the same analysis as before to the lightest and recoiling pairs from the 4 pion sample.

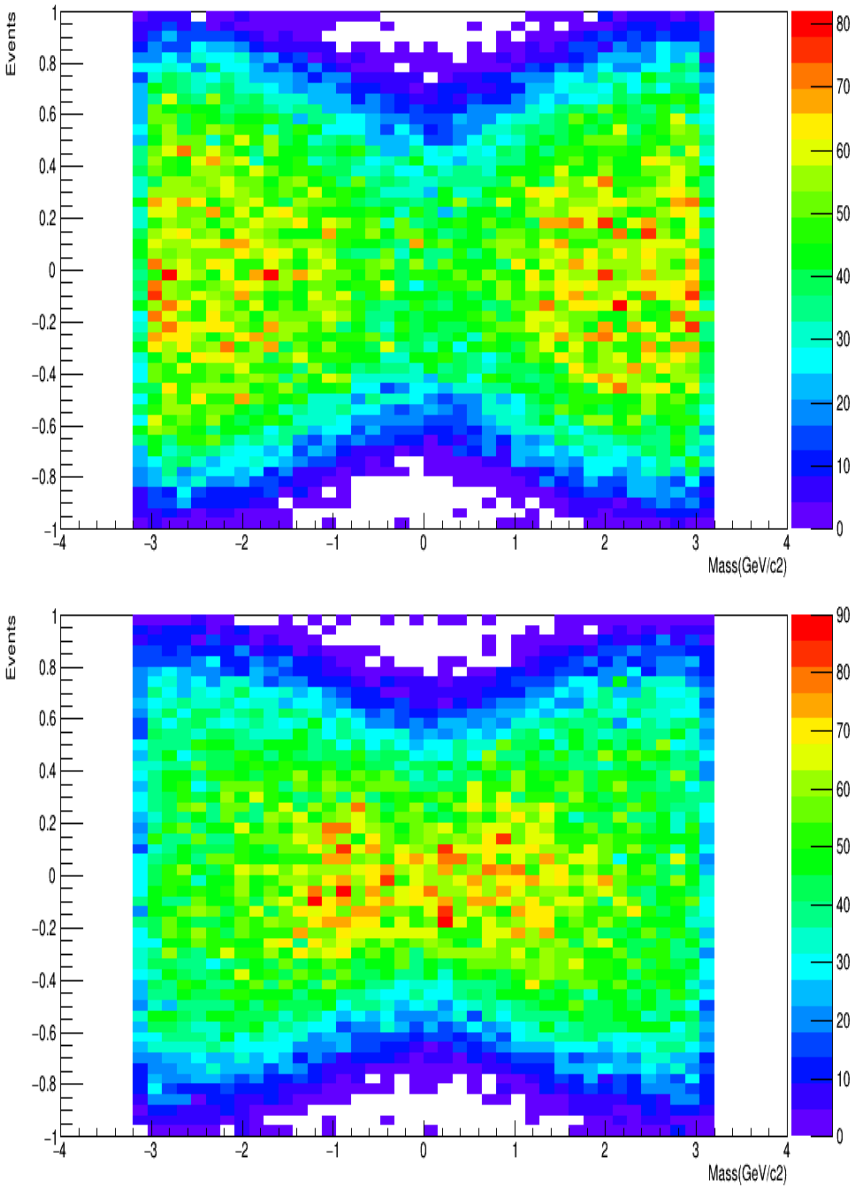


Figure 4.48: The figure above represents the angular distribution of the lighter pion pair and the figure below the angular distribution of the recoiling.

Finally, it should be noted that these last two plots were carried out with the standard four-pion considerations, which give us the opportunity to implement in the future a study of two-dimensional distributions in the azimuthal and polar angles within the

Collins-Soper frame of reference.

## 4.7 Results for $\pi^+\pi^-\pi^+\pi^-$

Our invariant mass distribution for pi+pi-pi+pi- is comparable with the reported by STAR experiment [4] in ultra-peripheral collisions at RHIC energies.

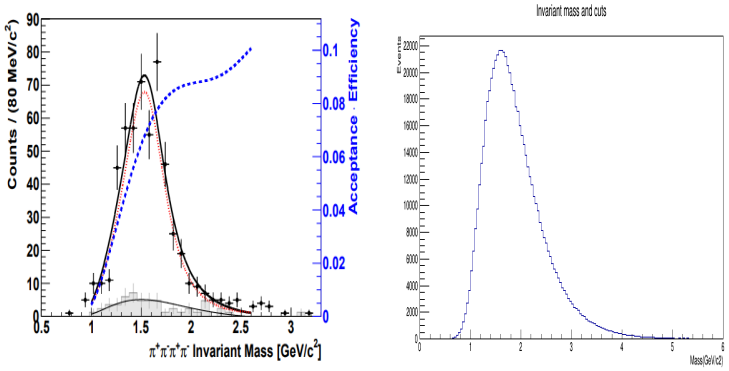


Figure 4.49: The image on the left corresponds to the graph obtained by the STAR detector [4] and the one on the right is the invariant mass spectrum with the IM + PID + Pt + !V0 + !AD + Vtx + VtxChi2 cut.

From both spectra we can highlight the clear similarity between both distributions with a clear visible peak around 1.5 GeV.

# Chapter 5

# Summary and Reflections

The analysis elaborated from the experimental sample has obtained good results in both studies, in the case of the two pions it was possible to establish a qualitative comparison between the invariant mass spectra and the results obtained by the COMPASS experiment in 2009 and Run 1 of the ALICE experiment, where, in addition to finding similarities between them, some resonances were identified as $\rho^0(770)$ , $f_0(980)$ and $f_2(1270)$ which are considered as possible glueball candidates.

On the other hand, the study of the angular distributions for the azimuthal and polar angles allowed us to compare qualitatively with those proposed in the article **Extracting the Pomeron-Pomeron-$f_2(1270)$ coupling in the $pp \longrightarrow pp\pi^+\pi^-$ reaction through the angular distribution of the pions** by Lebiedowicks P. and others, from them it was possible to observe the similarity that exists between those reconstructed with the experimental sample and those presented for the pions pair continuum and for the coupling of $ppf_2(1270)$ given by j=2, where the latter could be compared with the angular distributions obtained with the considerations in mass, transverse momentum and in the *eta* variable. It is important to note that the changes in the angular distributions were more appreciated when the cut was performed in the mass range and in the *eta* variable.

The four-pion analysis performed for 2017 shows a similar invariant mass spectrum as

the one reported by STAR experiment, with the difference that the STAR detector reported its four-pion spectrum for ultraperipheral collisions, while the one reconstructed and presented in this thesis obtained from central production diffractive processes collected in proton-proton collisions at 13 teV. In addition, it is important to note that the angular distributions presented for the light pion pair and recoiling provide the opportunity to implement a study of four-body angular distributions in the future.

The next steps in the scopus of this analysis are the study of the whole 2018 data sample for 2 and 4 pion events. Our results suggest that with the forthcoming data from LHC Run 3, ALICE will be in an excellent position to increase the statistics to improve the analysis presented in this thesis. Furthermore, our results shows that the 2 pion system reconstructed by ALICE (this work) could be comparable with the theorical prediction that assumes the production of $f_2(1250)$ resonance via a double pomeron exchange in diffractive processes at LHC energies.

# Bibliography


[1] *ALICE*. https://home.cern/science/experiments/alice, Retrieved: 18/05/2022.

[2] *ALICE-Collaboration*. https://alice-collaboration.web.cern.ch, Retrieved: 18/05/2022.

[3] *https://cds.cern.ch/record/2157235/plots*. Retrieved: 28/05/2022, 20:00.

[4] Abelev, B. . *Observation of $\pi + \pi - \pi + \pi-$ Photoproduction in Ultra-Peripheral Heavy Ion Collisions at $\sqrt{s_{NN}} = 200$ GeV at the STAR Detector*. arxiv.org/pdf/0912.0604.v2 . p.9, 2013.

[5] ALICE Collaboration (B. Abelev, A. Fernández Tellez, M. R. C. e. a. *Measurement of inelastic, single and double diffraction cross sections in proton-proton collisions at the LHC with ALICE*. Eur. Phys. J. C. 73, 2456, 2013.

[6] ALICE Collaboration (B. Abelev, A. Fernández Tellez, M. R. C. e. a. *Performance of the ALICE Experiment at the CERN-LHC*. Int. J. Mod. Phys. A 29, 1430044, 2014.

[7] Austregesilo, A. *Central Production of Two-Pseudoscalar Final States at COMPASS*. arxiv.org/pdf/1310.3190.v1. p.4, 2013.

[8] Barone, V. y Predazzi, E. *High-Energy Particle Driffraction*. Springer, 2002.

[9] Collins, P. *An Introduction to Regge Theory and High Energy Physics*. Cambridge University Press, Cambridge, 1977.

[10] Cotăescu, I.I., C. C. . S. C. *Partial wave analysis of the Dirac fermions scattered from Schwarzschild black holes.* Eur. Phys. J. C 76, 102, 2016.

[11] Dudley, C. *What is a Resonance Particle?* https://webhome.phy.duke.edu/ kolena/modern/dudley.html.

[12] et al, A. L. H. *Partial wave analysis of oriented collisions.* . Phys. B: At. Mol. Opt. Phys. 51, 015203, 2018.

[13] Griffiths, D. J. *Introduction to Quantum Mechanics.* 2nd Edi-tion; Pearson Education, 2005.

[14] Jackson, D. *Classical Electrodynamics.* Berkeley: JOHN WILEY SONS, INC., 1998.

[15] Kim, T., and Hwan K., J. *Partial wave analysis of centrally produced $\pi + \pi-$ system in p-p collisions at $\sqrt{s} = 7$ TeV.* URL: https://home.cern/science/experiments/alice, 2017.

[16] Lebiedowicz, P., N. O., and A., S. *Extracting the pomeron-pomeron-$f_2(1270)$ coupling in the $pp \longrightarrow pp\pi^+\pi^-$ reaction through angular distributions of the pions.* arXiv:1901.07788v2, 2019.

[17] M., T. *Study of QCD and diffraction with the ATLAS detector at the LHC.* Université Paris-Sud 11, 2013.

[18] Maestre, J. A. *Details on the Collins-Soper reference frame and lepton angular distributions in electroweak vector boson production at hadron colliders.* Editorial CIEMAT, 2020.

[19] Revol, J. *Diffractive Physics at the CERN Large Hadron Collider.* Nucl. Phys. A, 862-863, 212-222, 2011.

[20] Richard A. Arndt, Ron L. Workman, Z. L., and Roper, L. D. *Partial-wave analysis of pion photoproduction.* Phys. Rev. C 42, 1853, 1990.

[21] T. Abbott, L. K., and Remsberg, L. *Rapidity and Invariant Cross Sections.* Brookhaven National Laboratory, Upton, NY 11975.

[22] Toki, W. *Search for Glueballs.* Department oh Physics, Colorado State University, 1996.

[23] Tsipenyuk, A. *Fundamentals of Partial Wave Analysis and an Application to Heavy-Meson Decay using the No-U-Turn Sampler.* Technische Universität München, 2016.

[24] Villatoro, A. *Detection and discrimation of diffractive events with ALICE-LHC at CERN. Tesis Doctoral.* Benemérita Universidad Autónoma de Puebla.Puebla, 2019.

[25] Zinonos, Z. *Tests of the Standard Model of Particles.* Max-Planck-Institut fur Physik, TUM, 2017.